Loyola University Chicago
Loyola eCommons

Physics: Faculty Publications and Other Works

Faculty Publications and Other Works by Department

4-16-2021

A search for time-dependent astrophysical neutrino emission with icecube data from 2012 to 2017

R. Abbasi
Loyola University of Chicago

M. Ackermann
Deutsches Elektronen-Synchrotron (DESY)

J. Adams
University of Canterbury

J. A. Aguilar
Université Libre de Bruxelles

M. Ahlers
Niels Bohr Institutet

See next page for additional authors

Follow this and additional works at: https://ecommons.luc.edu/physics_facpubs

Recommended Citation

Abbasi, R.; Ackermann, M.; Adams, J.; Aguilar, J. A.; Ahlers, M.; Ahrens, M.; Alispach, C.; Alves, Jr A.; Amin, N. M.; Andeen, K.; Anderson, T.; Ansseau, I.; Anton, G.; Argüelles, C.; Axani, S.; Bai, X.; Balagopal V, A.; Barbano, A.; Barwick, S. W.; Bastian, B.; Basu, V.; Baum, V.; Baur, S.; Bay, R.; and Beatty, J. J., "A search for time-dependent astrophysical neutrino emission with icecube data from 2012 to 2017" (2021). *Physics: Faculty Publications and Other Works*. 95.
https://ecommons.luc.edu/physics_facpubs/95

This Article is brought to you for free and open access by the Faculty Publications and Other Works by Department at Loyola eCommons. It has been accepted for inclusion in Physics: Faculty Publications and Other Works by an authorized administrator of Loyola eCommons. For more information, please contact ecommons@luc.edu.

Authors

R. Abbasi, M. Ackermann, J. Adams, J. A. Aguilar, M. Ahlers, M. Ahrens, C. Alispach, Jr A. Alves, N. M. Amin, K. Andeen, T. Anderson, I. Ansseau, G. Anton, C. Argüelles, S. Axani, X. Bai, A. Balagopal V, A. Barbano, S. W. Barwick, B. Bastian, V. Basu, V. Baum, S. Baur, R. Bay, and J. J. Beatty

This article is available at Loyola eCommons: https://ecommons.luc.edu/physics_facpubs/95

The Astrophysical Journal, 911:67 (16pp), 2021 April 10 https://doi.org/10.3847/1538-4357/abe7e6
© 2021. The American Astronomical Society. All rights reserved.

A Search for Time-dependent Astrophysical Neutrino Emission with IceCube Data from 2012 to 2017

R. Abbasi[1], M. Ackermann[2], J. Adams[3], J. A. Aguilar[4], M. Ahlers[5], M. Ahrens[6], C. Alispach[7], A. A. Alves, Jr.[8], N. M. Amin[9], K. Andeen[10], T. Anderson[11], I. Ansseau[4], G. Anton[12], C. Argüelles[13], S. Axani[14], X. Bai[15], A. Balagopal V.[16], A. Barbano[7], S. W. Barwick[17], B. Bastian[2], V. Basu[16], V. Baum[18], S. Baur[4], R. Bay[19], J. J. Beatty[20,21], K.-H. Becker[22], J. Becker Tjus[23], C. Bellenghi[24], S. BenZvi[25], D. Berley[26], E. Bernardini[2,58], D. Z. Besson[27,59], G. Binder[19,28], D. Bindig[22], E. Blaufuss[26], S. Blot[2], S. Böser[18], O. Botner[29], J. Böttcher[30], E. Bourbeau[5], J. Bourbeau[16], F. Bradascio[2], J. Braun[16], S. Bron[7], J. Brostean-Kaiser[2], A. Burgman[29], R. S. Busse[31], M. A. Campana[32], C. Chen[33], D. Chirkin[16], S. Choi[34], B. A. Clark[35], K. Clark[36], L. Classen[31], A. Coleman[9], G. H. Collin[14], J. M. Conrad[14], P. Coppin[37], P. Correa[37], D. F. Cowen[11,38], R. Cross[25], P. Dave[33], C. De Clercq[37], J. J. DeLaunay[11], H. Dembinski[9], K. Deoskar[6], S. De Ridder[39], A. Desai[16], P. Desiati[16], K. D. de Vries[37], G. de Wasseige[37], M. de With[40], T. DeYoung[35], S. Dharani[30], A. Diaz[14], J. C. Díaz-Vélez[16], H. Dujmovic[8], M. Dunkman[11], M. A. DuVernois[16], E. Dvorak[15], T. Ehrhardt[18], P. Eller[24], R. Engel[8], J. Evans[26], P. A. Evenson[9], S. Fahey[16], A. R. Fazely[41], S. Fiedlschuster[12], A. T. Fienberg[11], K. Filimonov[19], C. Finley[6], L. Fischer[2], D. Fox[38], A. Franckowiak[2,23], E. Friedman[26], A. Fritz[18], P. Fürst[30], T. K. Gaisser[9], J. Gallagher[42], E. Ganster[30], S. Garrappa[2], L. Gerhardt[28], A. Ghadimi[43], C. Glaser[29], T. Glauch[24], T. Glüsenkamp[12], A. Goldschmidt[28], J. G. Gonzalez[9], S. Goswami[43], D. Grant[35], T. Grégoire[11], Z. Griffith[16], S. Griswold[25], M. Gündüz[23], C. Haack[24], A. Hallgren[29], R. Halliday[35], L. Halve[30], F. Halzen[16], M. Ha Minh[24], K. Hanson[16], J. Hardin[16], A. A. Harnisch[35], A. Haungs[8], S. Hauser[30], D. Hebecker[40], K. Helbing[22], F. Henningsen[24], E. C. Hettinger[35], S. Hickford[22], J. Hignight[44], C. Hill[45], G. C. Hill[46], K. D. Hoffman[26], R. Hoffmann[22], T. Hoinka[47], B. Hokanson-Fasig[16], K. Hoshina[16,60], F. Huang[11], M. Huber[24], T. Huber[8], K. Hultqvist[6], M. Hünnefeld[47], R. Hussain[16], S. In[34], N. Iovine[4], A. Ishihara[45], M. Jansson[6], G. S. Japaridze[48], M. Jeong[34], B. J. P. Jones[49], R. Joppe[30], D. Kang[8], W. Kang[34], X. Kang[32], A. Kappes[31], D. Kappesser[18], T. Karg[2], M. Karl[24], A. Karle[16], U. Katz[12], M. Kauer[16], M. Kellermann[30], J. L. Kelley[16], A. Kheirandish[11], J. Kim[34], K. Kin[45], T. Kintscher[2], J. Kiryluk[50], S. R. Klein[19,28], R. Koirala[9], H. Kolanoski[40], L. Köpke[18], C. Kopper[35], S. Kopper[43], D. J. Koskinen[5], P. Koundal[8], M. Kovacevich[32], M. Kowalski[2,40], K. Krings[24], G. Krückl[18], N. Kurahashi[32], A. Kyriacou[46], C. Lagunas Gualda[2], J. L. Lanfranchi[11], M. J. Larson[26], F. Lauber[22], J. P. Lazar[13,16], K. Leonard[16], A. Leszczyńska[8], Y. Li[11], Q. R. Liu[16], E. Lohfink[18], C. J. Lozano Mariscal[31], L. Lu[45], F. Lucarelli[7], A. Ludwig[35,51], W. Luszczak[16], Y. Lyu[19,28], W. Y. Ma[2], J. Madsen[16], K. B. M. Mahn[35], Y. Makino[16], P. Mallik[30], S. Mancina[16], I. C. Mariş[4], R. Maruyama[52], K. Mase[45], F. McNally[53], K. Meagher[16], A. Medina[21], M. Meier[45], S. Meighen-Berger[24], J. Merz[30], J. Micallef[35], D. Mockler[4], G. Momenté[18], T. Montaruli[7], R. W. Moore[44], R. Morse[16], M. Moulai[14], R. Naab[2], R. Nagai[45], U. Naumann[22], J. Necker[2], L. V. Nguyễn[35], H. Niederhausen[24], M. U. Nisa[35], S. C. Nowicki[35], D. R. Nygren[28], A. Obertacke Pollmann[22], M. Oehler[8], A. Olivas[26], E. O'Sullivan[29], H. Pandya[9], D. V. Pankova[11], N. Park[16], G. K. Parker[49], E. N. Paudel[9], P. Peiffer[18], C. Pérez de los Heros[29], S. Philippen[30], D. Pieloth[47], S. Pieper[22], A. Pizzuto[16], M. Plum[10], Y. Popovych[30], A. Porcelli[39], M. Prado Rodriguez[16], P. B. Price[19], B. Pries[35], G. T. Przybylski[28], C. Raab[4], A. Raissi[3], M. Rameez[5], K. Rawlins[54], I. C. Rea[24], A. Rehman[9], R. Reimann[30], M. Renschler[8], G. Renzi[4], E. Resconi[24], S. Reusch[2], W. Rhode[47], M. Richman[32], B. Riedel[16], S. Robertson[19,28], G. Roellinghoff[34], M. Rongen[30], C. Rott[34], T. Ruhe[47], D. Ryckbosch[39], D. Rysewyk Cantu[35], I. Safa[13,16], S. E. Sanchez Herrera[35], A. Sandrock[47], J. Sandroos[18], M. Santander[43], S. Sarkar[55], S. Sarkar[44], K. Satalecka[2], M. Scharf[30], M. Schaufel[30], H. Schieler[8], P. Schlunder[47], T. Schmidt[26], A. Schneider[16], J. Schneider[12], F. G. Schröder[8,9], L. Schumacher[30], S. Sclafani[32], D. Seckel[9], S. Seunarine[56], S. Shefali[30], M. Silva[16], B. Smithers[49], R. Snihur[16], J. Soedingrekso[47], D. Soldin[9], G. M. Spiczak[56], C. Spiering[2,58], J. Stachurska[2], M. Stamatikos[21], T. Stanev[9], R. Stein[2], J. Stettner[30], A. Steuer[18], T. Stezelberger[28], R. G. Stokstad[28], T. Stuttard[5], G. W. Sullivan[26], I. Taboada[33], F. Tenholt[23], S. Ter-Antonyan[41], S. Tilav[9], F. Tischbein[30], K. Tollefson[35], L. Tomankova[23], C. Tönnis[57], S. Toscano[4], D. Tosi[16], A. Trettin[2], M. Tselengidou[12], C. F. Tung[33], A. Turcati[24], R. Turcotte[8], C. F. Turley[11], J. P. Twagirayezu[35], B. Ty[16], M. A. Unland Elorrieta[31], J. Vandenbroucke[16], D. van Eijk[16], N. van Eijndhoven[37], D. Vannerom[14], J. van Santen[2], S. Verpoest[39], M. Vraeghe[39], C. Walck[6], A. Wallace[46], T. B. Watson[49], C. Weaver[35], A. Weindl[8], M. J. Weiss[11], J. Weldert[18], C. Wendt[16], J. Werthebach[47], M. Weyrauch[8], B. J. Whelan[46], N. Whitehorn[35,51], K. Wiebe[18], C. H. Wiebusch[30], D. R. Williams[43], M. Wolf[24], K. Woschnagg[19], G. Wrede[12], J. Wulff[23], X. W. Xu[41], Y. Xu[50], J. P. Yanez[44], S. Yoshida[45], T. Yuan[16], and Z. Zhang[50]

IceCube Collaboration

[1] Department of Physics, Loyola University Chicago, Chicago, IL 60660, USA
[2] DESY, D-15738 Zeuthen, Germany
[3] Dept. of Physics and Astronomy, University of Canterbury, Private Bag 4800, Christchurch, New Zealand
[4] Université Libre de Bruxelles, Science Faculty CP230, B-1050 Brussels, Belgium
[5] Niels Bohr Institute, University of Copenhagen, DK-2100 Copenhagen, Denmark
[6] Oskar Klein Centre and Dept. of Physics, Stockholm University, SE-10691 Stockholm, Sweden
[7] Département de physique nucléaire et corpusculaire, Université de Genève, CH-1211 Genève, Switzerland
[8] Karlsruhe Institute of Technology, Institute for Astroparticle Physics, D-76021 Karlsruhe, Germany
[9] Bartol Research Institute and Dept. of Physics and Astronomy, University of Delaware, Newark, DE 19716, USA

[10] Department of Physics, Marquette University, Milwaukee, WI, 53201, USA
[11] Dept. of Physics, Pennsylvania State University, University Park, PA 16802, USA
[12] Erlangen Centre for Astroparticle Physics, Friedrich-Alexander-Universität Erlangen-Nürnberg, D-91058 Erlangen, Germany
[13] Department of Physics and Laboratory for Particle Physics and Cosmology, Harvard University, Cambridge, MA 02138, USA
[14] Dept. of Physics, Massachusetts Institute of Technology, Cambridge, MA 02139, USA
[15] Physics Department, South Dakota School of Mines and Technology, Rapid City, SD 57701, USA
[16] Dept. of Physics and Wisconsin IceCube Particle Astrophysics Center, University of Wisconsin–Madison, Madison, WI 53706, USA
[17] Dept. of Physics and Astronomy, University of California, Irvine, CA 92697, USA
[18] Institute of Physics, University of Mainz, Staudinger Weg 7, D-55099 Mainz, Germany
[19] Dept. of Physics, University of California, Berkeley, CA 94720, USA
[20] Dept. of Astronomy, Ohio State University, Columbus, OH 43210, USA
[21] Dept. of Physics and Center for Cosmology and Astro-Particle Physics, Ohio State University, Columbus, OH 43210, USA
[22] Dept. of Physics, University of Wuppertal, D-42119 Wuppertal, Germany
[23] Fakultät für Physik & Astronomie, Ruhr-Universität Bochum, D-44780 Bochum, Germany
[24] Physik-department, Technische Universität München, D-85748 Garching, Germany
[25] Dept. of Physics and Astronomy, University of Rochester, Rochester, NY 14627, USA
[26] Dept. of Physics, University of Maryland, College Park, MD 20742, USA
[27] Dept. of Physics and Astronomy, University of Kansas, Lawrence, KS 66045, USA
[28] Lawrence Berkeley National Laboratory, Berkeley, CA 94720, USA
[29] Dept. of Physics and Astronomy, Uppsala University, Box 516, SE-75120 Uppsala, Sweden
[30] III. Physikalisches Institut, RWTH Aachen University, D-52056 Aachen, Germany
[31] Institut für Kernphysik, Westfälische Wilhelms-Universität Münster, D-48149 Münster, Germany
[32] Dept. of Physics, Drexel University, 3141 Chestnut Street, Philadelphia, PA 19104, USA
[33] School of Physics and Center for Relativistic Astrophysics, Georgia Institute of Technology, Atlanta, GA 30332, USA
[34] Dept. of Physics, Sungkyunkwan University, Suwon 16419, Korea
[35] Dept. of Physics and Astronomy, Michigan State University, East Lansing, MI 48824, USA
[36] SNOLAB, 1039 Regional Road 24, Creighton Mine 9, Lively, ON, P3Y 1N2, Canada
[37] Vrije Universiteit Brussel (VUB), Dienst ELEM, B-1050 Brussels, Belgium
[38] Dept. of Astronomy and Astrophysics, Pennsylvania State University, University Park, PA 16802, USA
[39] Dept. of Physics and Astronomy, University of Gent, B-9000 Gent, Belgium
[40] Institut für Physik, Humboldt-Universität zu Berlin, D-12489 Berlin, Germany
[41] Dept. of Physics, Southern University, Baton Rouge, LA 70813, USA
[42] Dept. of Astronomy, University of Wisconsin–Madison, Madison, WI 53706, USA
[43] Dept. of Physics and Astronomy, University of Alabama, Tuscaloosa, AL 35487, USA
[44] Dept. of Physics, University of Alberta, Edmonton, Alberta, T6G 2E1, Canada
[45] Dept. of Physics and Institute for Global Prominent Research, Chiba University, Chiba 263-8522, Japan
[46] Department of Physics, University of Adelaide, Adelaide, 5005, Australia
[47] Dept. of Physics, TU Dortmund University, D-44221 Dortmund, Germany
[48] CTSPS, Clark-Atlanta University, Atlanta, GA 30314, USA
[49] Dept. of Physics, University of Texas at Arlington, 502 Yates St., Science Hall Rm 108, Box 19059, Arlington, TX 76019, USA
[50] Dept. of Physics and Astronomy, Stony Brook University, Stony Brook, NY 11794-3800, USA
[51] Department of Physics and Astronomy, UCLA, Los Angeles, CA 90095, USA
[52] Dept. of Physics, Yale University, New Haven, CT 06520, USA
[53] Department of Physics, Mercer University, Macon, GA 31207-0001, USA
[54] Dept. of Physics and Astronomy, University of Alaska Anchorage, 3211 Providence Dr., Anchorage, AK 99508, USA
[55] Dept. of Physics, University of Oxford, Parks Road, Oxford OX1 3PU, UK
[56] Dept. of Physics, University of Wisconsin, River Falls, WI 54022, USA
[57] Institute of Basic Science, Sungkyunkwan University, Suwon 16419, Korea
Received 2020 December 2; revised 2021 February 16; accepted 2021 February 17; published 2021 April 16

Abstract

High-energy neutrinos are unique messengers of the high-energy universe, tracing the processes of cosmic ray acceleration. This paper presents analyses focusing on time-dependent neutrino point-source searches. A scan of the whole sky, making no prior assumption about source candidates, is performed, looking for a space and time clustering of high-energy neutrinos in data collected by the IceCube Neutrino Observatory between 2012 and 2017. No statistically significant evidence for a time-dependent neutrino signal is found with this search during this period, as all results are consistent with the background expectation. Within this study period, the blazar 3C 279, showed strong variability, inducing a very prominent gamma-ray flare observed in 2015 June. This event motivated a dedicated study of the blazar, which consists of searching for a time-dependent neutrino signal correlated with the gamma-ray emission. No evidence for a time-dependent signal is found. Hence, an upper limit on the neutrino fluence is derived, allowing us to constrain a hadronic emission model.

Key words: Particle astrophysics – High-energy astrophysics – Cosmic ray sources

1. Introduction

The cosmic ray energy spectrum is observed from the sub-GeV region to ultra-high energies in the 10^{20} eV range. While the lowest-energy cosmic rays are thought to originate from Galactic supernova explosions (Baade & Zwicky 1934),

[58] Also at Università di Padova, I-35131 Padova, Italy.
[59] Also at National Research Nuclear University, Moscow Engineering Physics Institute (MEPhI), Moscow 115409, Russia.
[60] Also at Earthquake Research Institute, University of Tokyo, Bunkyo, Tokyo 113-0032, Japan.

extragalactic objects, such as gamma-ray bursts and active galactic nuclei (Waxman & Bahcall 1999; Mannheim et al. 2001), are candidates to explain the highest-energy part of the spectrum. However, none of these hypotheses has been experimentally verified, and the origin of cosmic rays remains mostly unknown.

At very high energy, a large-scale anisotropy in cosmic ray directions has been observed (Aab et al. 2017), and some indication of correlation between cosmic ray arrival direction and γ-ray sources has been found (Aab et al. 2018). However, it remains difficult to infer the exact origin of cosmic rays from their directional distribution, because they are deflected by magnetic fields on their way to Earth. More precise information can be obtained thanks to secondary particles created in the vicinity of cosmic ray sources. Indeed, cosmic rays interact with gas and radiation near their accelerating sites, leading to the production of charged and neutral pions, which in turn produce neutrinos and photons. Those two particles are indirect messengers that have the potential to point back at cosmic ray sources, as they are both neutral and thus not sensitive to magnetic fields. However, photon detection alone is delicate; many different phenomena can be responsible for their emission, and the photons detected at Earth or by satellites are not necessarily the same as the ones that were produced by cosmic ray interaction. Photons are also produced in leptonic processes such as bremsstrahlung, inverse Compton scattering, and synchrotron radiation, which would be overlaid upon the photons produced in hadronic processes, alongside the neutrinos. Neutrinos, on the other hand, can only have hadronic origin. They are powerful messengers, because they pass through the universe basically undisturbed. At the same time, this implies a challenge for their detection. The observation of both neutrinos and gamma-rays from a same source is a smoking gun to trace cosmic ray sources.

The IceCube detector has been able to address the neutrino challenge, and has reported the detection of a cosmic neutrino flux at the level of few events per year above $\sim$50 TeV on top of the softer atmospheric neutrino and muon background (Aartsen et al. 2013a, 2014b, 2015a). Even if the sources of those high-energy neutrinos are still unknown, some evidence for possible candidates started to show up in recent observations. In 2017, a very high-energy neutrino event, IceCube-170922A, was detected. It triggered an alert and a follow-up in the event's direction, and was realized in various photon bands by several independent experiments. Evidence for a blazar in a flaring state, TXS 0506+056, consistent with the direction of the neutrino event, was first claimed by the *Fermi* gamma-ray satellite, then confirmed by the MAGIC telescopes and also other high-energy gamma-ray experiments (Aartsen et al. 2018a; Abeysekara et al. 2018). The analysis reported a coincidence between IceCube-170922A and the flare of TXS 0506+056 that was inconsistent with a background fluctuation at the level of 3σ. In addition to that, a time-dependent search, similar to what is described in this paper, was conducted on 9.5 yr of archival data and revealed a 3.5σ evidence for neutrino emission in the direction of this blazar during a $\sim$110-day period in 2014–2015 (Aartsen et al. 2018b), this time not accompanied by an observed blazar flare. Those observations combined together make TXS 0506+056 the first blazar associated with a significant neutrino excess. However, only $\sim$1% of the diffuse flux previously observed in IceCube can be attributed to this single source (Aartsen et al. 2019).

In 2019, a search for astrophysical neutrino point-like sources was conducted on 10 yr of IceCube data. Several types of analysis were realized. Very interestingly, the scan of the whole sky, using neutrino-data only, revealed a clustering of high-energy neutrinos, exceeding the background expectation at the level of 2.9σ, at a location in the sky coinciding with the Seyfert II galaxy NGC 1068 (Aartsen et al. 2019). In addition to the all-sky analysis, a catalog of sources observed in gamma-rays was constructed. All sources considered together, the catalog of the Northern Hemisphere was found to be inconsistent with a background-only hypothesis at 3.3σ. This result is mostly due to excesses found in the neutrino data in the directions of the Seyfert II galaxy NGC 1068, the blazar TXS 0506+056, and the BL Lacs PKS 1424+240 and GB6 J1542+6129. Those results, together with flaring observations from the direction of TXS 0506+056, motivate searches for neutrino sources whose emission is time-dependent, which can provide complementary information to the time-integrated analyses.

In this paper, we illustrate a dedicated search for time-dependent signals performed on IceCube data from 2012 to 2017. This search consists of looking for a space and time clustering of high-energy neutrinos above 1 TeV, scanning the whole sky. It updates the previous search, which used IceCube data from 2008 to 2012 (Aartsen et al. 2015b). Time-dependent studies are relevant because, for flares below about 100 days, they have a better discovery potential than time-integrated searches (Aartsen et al. 2015b).

One time-variable source of special interest is the blazar 3C 279, a frequently studied flat spectrum radio quasar (FSRQ) at redshift $z = 0.536$. It has been observed since the end of the 1980s in radio (Aller et al. 1987), optical and infrared (Kidger et al. 1990), and X-ray bands (Makino et al. 1989), and the first gamma-ray observation was achieved in 1991 by the EGRET experiment (Hartman et al. 1992; Maraschi et al. 1992). More recently, the Fermi-Large Area Telescope (LAT) detected two prominent gamma-ray flares, in December 2013 (Hayashida et al. 2015) and on 2015 June 16, the latter being exceptionally bright (Cutini 2015; Hayashida et al. 2015), thus making this blazar one of the brightest objects ever observed at such high energies and such distances. For one day, the Fermi-LAT experiment detected a flux exceeding the steady flux of the source by more than forty times. This is the historically highest gamma-ray luminosity observed from 3C 279, including also past EGRET observations, with a γ-ray isotropic luminosity reaching $\sim 10^{49}$ erg s^{-1}. Moreover, a minute-timescale variability of the blazar is reported (Ackermann et al. 2016), with the flux doubling in less than 10 minutes, which is a very rare event. This allows us to explore compatibility of observations with purely leptonic standard models of FSRQs, in which gamma-rays are produced by external radiation comptonization (ERC; Sikora et al. 2009) or hadronic models. In the ERC model, depending on assumptions, a high Lorentz factor ($>$50) and extremely low jet magnetization or a Lorentz factor of 120 are required (Ackermann et al. 2016). An alternative leptonic model would imply a magnetically dominated jet still with a high Lorentz factor of about 25 (Ackermann et al. 2016). In this paper, we focus on hadronic models, which, as explained above, foresee interactions of protons with ordinary matter or radiation. In particular, we constrain the model in Halzen & Kheirandish (2016). The analysis of IceCube data, driven by the Fermi-LAT gamma-ray data, gives us an opportunity to test this model for the 2015 flare of 3C 279.

Table 1
Summary of the Data Used in the Reported Analyses

Analysis	Number of Throughgoing Tracks	Number MESE Tracks	Number GFU Tracks	Start Day	End Day	Lifetime (days)
All-sky scan I	338588	603	⋯	15.05.2012	18.05.2015	1057.54
All-sky scan II	⋯	⋯	571595	24.04.2015	01.11.2017	886.90
3C 279 flare analysis	3429	6	⋯	11.06.2015	22.06.2015	12.04

Note. Each line corresponds to one of the analyses, with the columns giving the specific data selection used, the number of tracks included, the start and end dates of the data, and the livetime of the data.

2. IceCube Detector and Data Sample

The IceCube detector is a cubic kilometer volume of instrumented ice located at the geographic South Pole. Its construction was completed in the austral summer 2010–2011. The detector consists of 86 strings, each holding 50 digital optical modules (DOMs) deployed at a depth between 1450 and 2450 m below the ice surface. The DOMs are spaced vertically by 17 m and each one hosts a 10 inch photomultiplier tube (Abbasi et al. 2010) and associated electronics (Abbasi et al. 2009) protected from the high pressure by a glass sphere. The horizontal separation between strings is 125 m. The detection is indirect, i.e., neutrinos interact with the Antarctic ice and produce secondary charged particles such as muons or electrons. Photomultiplier tubes (PMTs) in the DOMs observe Cherenkov radiation from those charged particles. The PMT signals are digitized in the DOMs, and transmitted to the surface.

Muon neutrinos can undergo charged-current interactions in the vicinity of or inside the instrumented region, resulting in muon tracks. Cascades originate from charged-current interactions of ν_e and ν_τ and from neutral-current interactions of all neutrino flavors. Track-like events have an angular resolution typically $\leqslant 0\overset{\circ}{.}8$ at $\sim$TeV energies and poor energy resolution on the order of a factor of two, while cascade events have about 15% deposited energy resolution, but only 10° angular resolution above some tens of TeV (Aartsen et al. 2014a). The analyses reported in this paper rely on good pointing capabilities and therefore use a sample of muon-track events. Neutrino event candidates arriving from the Northern Hemisphere (upgoing events) are mostly composed of misreconstructed downgoing muon events and of atmospheric neutrinos with energies above about 100 GeV. The latter constitute the dominant background in this hemisphere. The Southern Hemisphere is dominated by downgoing atmospheric muons. Therefore a higher energy threshold is applied to reduce them (Aartsen et al. 2017a).

The event selections used in the time-dependent analysis are different for the first 3 yr and the last 2.5 yr of data. Therefore, the two data sets are treated independently and the analysis is performed separately on each of them. Both data sets were recorded with the full configuration of IceCube. The all-sky scan uses a sample of about 3.5×10^5 good quality tracks ("through-going tracks") in the Southern and the Northern Hemispheres collected from 2012 May to 2015 May. For a detailed description of the event sample, see Aartsen et al. (2014c). To this sample, the Medium Energy Starting Events (MESE) lower-energy sample is also added (Aartsen et al. 2016). The MESE downgoing sample is selected by eliminating tracks, mostly due to atmospheric muons, starting outside a fiducial volume inside the instrumented region. In this way, it is possible to select neutrino events with their vertex in the fiducial region.

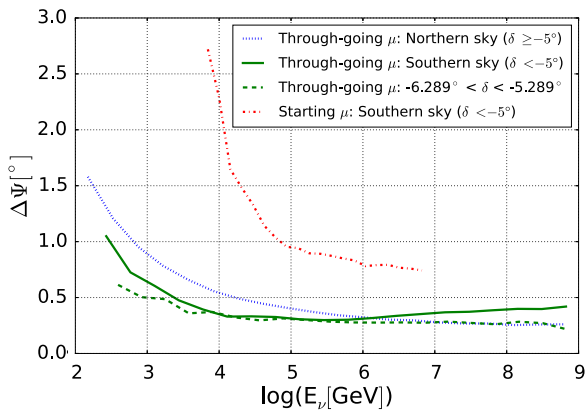

Figure 1. Median angular resolution (defined as the median angle between the reconstructed muon track and the parent neutrino direction from simulation) as a function of neutrino energy for the throughgoing muon tracks data set shown for northern declinations (dashed blue line), for southern declinations (solid green line), for a decl. band of 1° around 3C 279 decl. (dashed green line), and for the starting muon tracks (MESE) data set (dashed red line).

From 2015 April to 2017 November, a slightly different selection of muon tracks is used: the real-time event selection developed for the gamma-ray follow-up (GFU) program (Aartsen et al. 2017b). This sample includes 5.7×10^5 tracks.

For the analysis of the blazar 3C 279, we use a subsample of 11 days of the throughgoing tracks and the MESE sample, centered around the bright flare of the blazar, which happened on 2015 June 16. Given that the data selection is the same, the background probability functions (see Section 3.2) for the blazar analysis were built based on the full period of data between 2012 and 2015. All samples are summarized in Table 1.

The performance of these analyses strongly depends on the pointing precision and the effective area, which are described in Abbasi et al. (2011b). The pointing accuracy is estimated through the median of the distribution of the angle between the true neutrino direction and the reconstructed muon obtained from Monte Carlo simulations as a function of energy. Figure 1 shows this angle for throughgoing tracks in both the southern (green) and the northern (dashed blue) sky, as well as for the decl. band of 1° around the blazar 3C 279 (dashed green line). Above 10 TeV, the resolution is below $0\overset{\circ}{.}5$. The MESE angular resolution is shown in red. It is worse than that for the throughgoing tracks, due to the fact that events starting inside the detector have a shorter lever arm.

The angular resolution of the GFU data set is very similar to the throughgoing tracks, and is shown in Aartsen et al. (2017b). The direction of the tracks is calculated through an iterative maximum likelihood method. The uncertainty of the

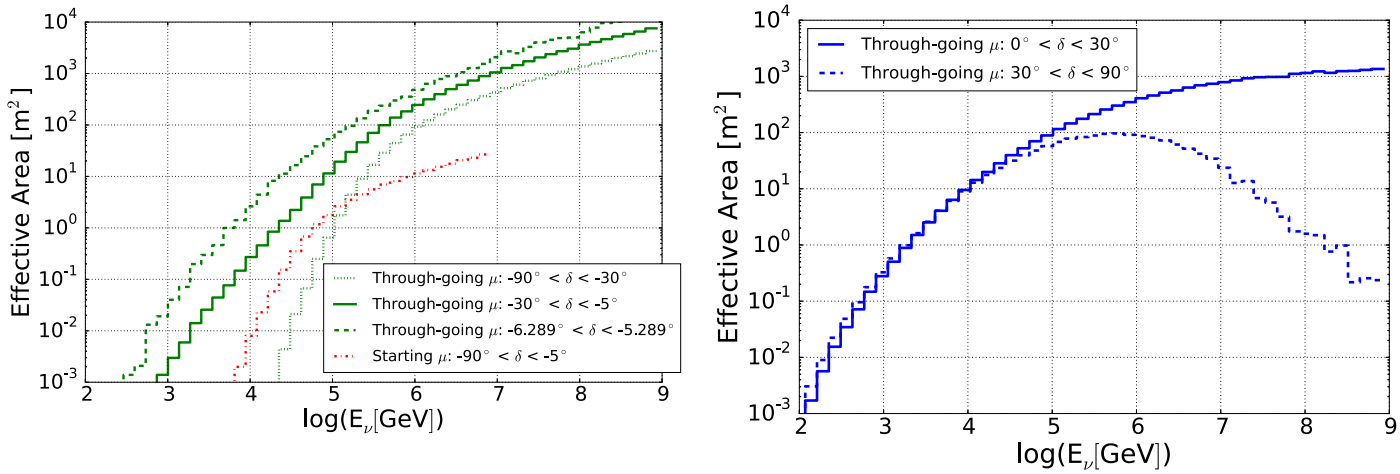

Figure 2. IceCube effective area as a function of neutrino energy for the throughgoing muon and starting muon (MESE) tracks data sets in the Southern Hemisphere (left) and for the throughgoing muon tracks data set in the Northern Hemisphere (right). The effective area is averaged over the solid angle in each decl. range.

reconstructed direction is estimated by the 1σ contour of the likelihood space around the minimum, which is estimated by a method fitting a two-dimensional parabola, called "paraboloid," to the likelihood landscape (Neunhoffer 2006). Figure 2 shows the effective area for the throughgoing and the MESE selections in the Southern Hemisphere (left) and in the Northern Hemisphere (right). The effective area is optimal at the location of 3C 279 (green line), since the source is very close to the horizon, where the Earth's absorption of high-energy neutrinos is negligible. The effective area for the GFU sample is comparable to that of the throughgoing tracks, as shown in Figure 3 of Aartsen et al. (2017b).

3. Analysis Method

The analysis is based on a standard point-source unbinned likelihood method that compares two hypotheses (Braun et al. 2008, 2010; Aartsen et al. 2015b):

1. $\mathcal{H}_0$, the null hypothesis, which assumes that all events in the data set are due to an isotropic background.
2. $\mathcal{H}_1$, which assumes that measured data are the result of the above described background in addition to a point-source astrophysical neutrino signal following a $\frac{dN}{dE} \propto E^{-\gamma}$ spectrum.

To quantify the probability that the data are not compatible with the null hypothesis, a test statistic is defined as:

$$TS = -2 \log \frac{P(\text{Data}|\mathcal{H}_0)}{P(\text{Data}|\mathcal{H}_1)}. \quad (1)$$

A larger TS value indicates a smaller compatibility with background. The probability of observing the data given a certain hypothesis, as written in the TS definition, is given by a likelihood function. The likelihood function contains parameters that are fitted in the analysis, and is defined as:

$$\mathcal{L}(\boldsymbol{x}_s, n_s, \gamma, ...) = \prod_{i=0}^{N} \left(\frac{n_s}{N} S_i + \left(1 - \frac{n_s}{N}\right) B_i\right), \quad (2)$$

where i runs over the number of events N, $\boldsymbol{x}_s$ is the source position, n_s is the number of signal events, γ is the source spectral index, and S_i and B_i, respectively, are the signal and the background probability density functions (PDFs).

The signal PDF is composed of a spatial, energy, and time PDF

$$S_i = P_i^{\text{sig}}(\sigma_i, \boldsymbol{x}_i|\boldsymbol{x}_s) \cdot \epsilon_i^{\text{sig}}(E_i, \delta_i|\gamma) \cdot T_i^{\text{sig}}, \quad (3)$$

where P_i^{sig} is the spatial PDF and ϵ_i^{sig} is the energy PDF, with σ_i the angular error, $\boldsymbol{x}_i$ the reconstructed direction, E_i the reconstructed energy, and δ_i the decl. of the event i. The spatial and energy PDFs are described in Aartsen et al. (2013b). The time PDF T_i^{sig} is specific to each analysis and will be described in the corresponding sections. The background PDF

$$B_i = P_i^{bkg}(\delta_i) \cdot \epsilon_i^{bkg}(E_i, \delta_i) \cdot T_i^{bkg} \quad (4)$$

has the same structure as the signal PDF and is described in Aartsen et al. (2013b).

The background spatial PDF $P_i^{bkg}(\delta_i)$ gives the density of atmospheric neutrinos and muons with respect to the decl. δ_i of the event i. It is uniform in R.A. when we consider data over a sufficiently long period. For short timescales, i.e., on the order of less than a day, a dependency in R.A. appears. This is caused by the fact that incoming neutrinos aligned with the strings of the detector are better reconstructed. This effect fades away with Earth rotation. In order to correctly treat short timescales, the R.A.-independent PDF is multiplied by a local coordinate distribution, $P_i^{bkg}(\phi_i, \cos\theta_i)$, which depends on both the zenith θ and the azimuth ϕ angle for each event i (Christov 2016). It should be noted that, at the South Pole, the relation between the zenith θ_i and the decl. δ_i is largely simplified to $\delta_i = -90° + \theta_i$. This is important because it means that the background variation at the local detector level (zenith) is equivalent to its variation in equatorial coordinates (decl.).

The energy PDF gives the probability of finding an event with measured energy E_i coming from the atmospheric background at the decl. of the event δ_i. Here, E_i is an energy proxy of the true neutrino energy based on the visible muon energy in the detector.

Finally, the time-dependent term of the background PDF is taken to be constant for the background, even though some seasonal variations are observed in the atmospheric event rates, due to changes of the atmosphere density (Abbasi et al. 2011a). These variations are at the level of ±15% of the rate of downgoing muons, but are greatly reduced for upgoing neutrinos coming from all latitudes across the Earth.

3.1. Time PDF of the All-sky Scans

The time-dependent term, $T_i^{\rm sig}$, is defined by a Gaussian function, with width σ_T and mean T_0:

$$T_i^{\rm sig} = \frac{1}{\sqrt{2\pi}\,\sigma_T} e^{\left(-\frac{(t_i - T_0)^2}{2\sigma_T^2}\right)}, \tag{5}$$

where t_i is the arrival time of the ith event. We also tested step functions to represent a flare, but the results did not change significantly.

In order to avoid an undesired bias of the fit toward short flares in a specific time period, a penalizing term $T/\sqrt{2\pi}\,\sigma_T$ is added to the original test statistics, as explained in Braun et al. (2010):

$$TS = -2\log\left[\frac{T}{\sqrt{2\pi}\,\hat{\sigma}_T} \times \frac{\mathcal{L}(n_s = 0)}{\mathcal{L}(\hat{n}_s, \hat{\gamma}_s, \hat{\sigma}_T, \hat{T}_0)}\right], \tag{6}$$

where $\hat{n}_s$, $\hat{\gamma}_s$, $\hat{\sigma}_T$, and $\hat{T}_0$ are the best-fit values of the parameters defined above.

The all-sky scan is realized by creating a $0\overset{\circ}{.}1 \times 0\overset{\circ}{.}1$ grid covering the whole sky, for declinations between $-85°$ to $+85°$ (not enough statistics are collected at the poles to apply the analysis there). The size of the grid is chosen to be smaller than the lower limit on the directional uncertainty of reconstructed tracks in IceCube (i.e., $0\overset{\circ}{.}2$), in order to identify the most compact objects in the sky. Moreover, it is necessary to use a fine grid in order to limit the distortion effects far from the equator.[61] The likelihood maximization, performed by fitting the free parameters, results in a *TS* value at each point of the sky grid.

This analysis is performed to determine the hottest spots in the northern and in the southern sky. In order to calculate the post-trial values of the *TS* for the hottest spots, we need to account for all the directions looked at. Because the sample is background-dominated, we use "pseudo-experiments" (trials) containing only background created by assigning a random location in the sky (R.A.) to each event (Aartsen et al. 2015b). By applying this procedure, which preserves the distributions in detector coordinates,[62] we make sure that no real signal that could potentially be contained in the sample remains in the trial sample.

The performance of the analysis can be estimated in terms of the sensitivity, defined as the average number of signal events (n_s) required so that 90% of the generated "equivalent" experiments have a *TS* greater than 50% of the background trials (i.e., where no signal events are injected on top of the background events), and in terms of the discovery potential, defined as the n_s required such that 50% of the trials have a *TS* greater than 5σ of the background distribution, i.e., a *p*-value of 3×10^{-7}. The average number of events observed from a source is directly related to its flux. The usual way of representing it in time-dependent analyses is through the time-integrated flux or through the fluence, which is the energy flux integrated over the time of the selected flare and over the energy interval, limited to the 5% and the 95% energy percentiles of the event sample (Aartsen et al. 2015b). Sensitivity and discovery potential in terms of n_s and time-integrated flux are shown in Figures 3 and 4 as a function of the logarithm of the duration of the flare for the periods from 2012 to 2015 (IC86 II-IV) and from 2015 to 2017 (IC86 V-VII), respectively.

3.2. Time PDF of 3C 279 Flare Analysis

The 3C 279 flare analysis is a *triggered* time-dependent point-source analysis, i.e., its search time window is determined by the flaring behavior of the source in gamma-rays. To build such an analysis, the gamma-ray information is combined with the neutrino information.

The gamma-ray emission of 3C 279 is recorded by Fermi-LAT, and its light curve, shown in Figure 5, is produced through an aperture photometry analysis[63] using a one-day binning. With the help of the analysis tools provided by the Fermi-LAT collaboration (*Fermi Science Tools v10r0p5* package[64]), open access photometric data from Fermi-LAT are downloaded. We use photons of the P8R3_SOURCE class with front and back conversions (Atwood et al. 2013). Those photons are then selected within 2° from the source, in order to further reduce the background. Photon events with zenith angles greater than 90° are excluded in order to avoid contamination due to the Earth's albedo. The photon energy range goes from 100 MeV to 500 GeV, as recommended by the Fermi-LAT collaboration.

After the light curve is created, it is denoised using the Bayesian block method (Scargle et al. 2013; Resconi et al. 2009). This allows us to remove the nonrepresentative fluctuations of the emission and to keep only the main features of the light curve. The light curve is modeled into blocks, each meant to represent a Poisson distribution with a constant mean, extending for a certain duration. The parameter of the Bayesian blocks, called $F_{\rm B}$, was set to 5, following a previous study on similar IceCube data (Aartsen et al. 2015b). A representation of a light curve turned into Bayesian blocks can be seen in Figure 6(a).

The gamma-ray and neutrinos data are analyzed over a period of 11 days, from 2015 June 11 to 2015 June 22, chosen to isolate the bright flare. The exact duration was selected based on a series of tests, aiming at maximizing the 5σ discovery potential (50% C.L.).

The likelihood function of this analysis follows the general form defined in Equation (2). The background PDF is described by Equation (4). The signal spatial and energy PDFs are defined in Equation (3), while the signal time PDF is specific to the triggered analysis. It depends on two parameters, fit in the likelihood maximization: the time lag, D_t, and the threshold, f_{th}.

The time lag describes a shift of the entire light curve in time, within the range of plus or minus half a day. This tolerance accounts for binning effects, e.g., when a photon flare is spread between contiguous one-day bins and not fully contained within them. While this is relevant for a light curve containing a single flare, such a binning effect would be averaged out when dealing with multiple flares.

[61] Since the grid is spherical, the pixels from the grid far from the equator are distorted and the distance between two pixels will be slightly larger than $0\overset{\circ}{.}1$. The coarser the grid, the more this effect will be enhanced.

[62] This is because the distribution of events is expected to be flat in R.A., due to the continuous flux of atmospheric neutrinos and muons, the Earth's rotation, and the fact that the acquisition is continuous and has no stop at a fixed time every day.

[63] Because of its fast execution and simplicity, this analysis method was preferred over a full-likelihood approach, despite the better flux precision of the latter, as the resulting light curve is only used in the time-dependent analysis for the variability of its relative flux (see Section 3.2).

[64] https://fermi.gsfc.nasa.gov/ssc/data/analysis/documentation/

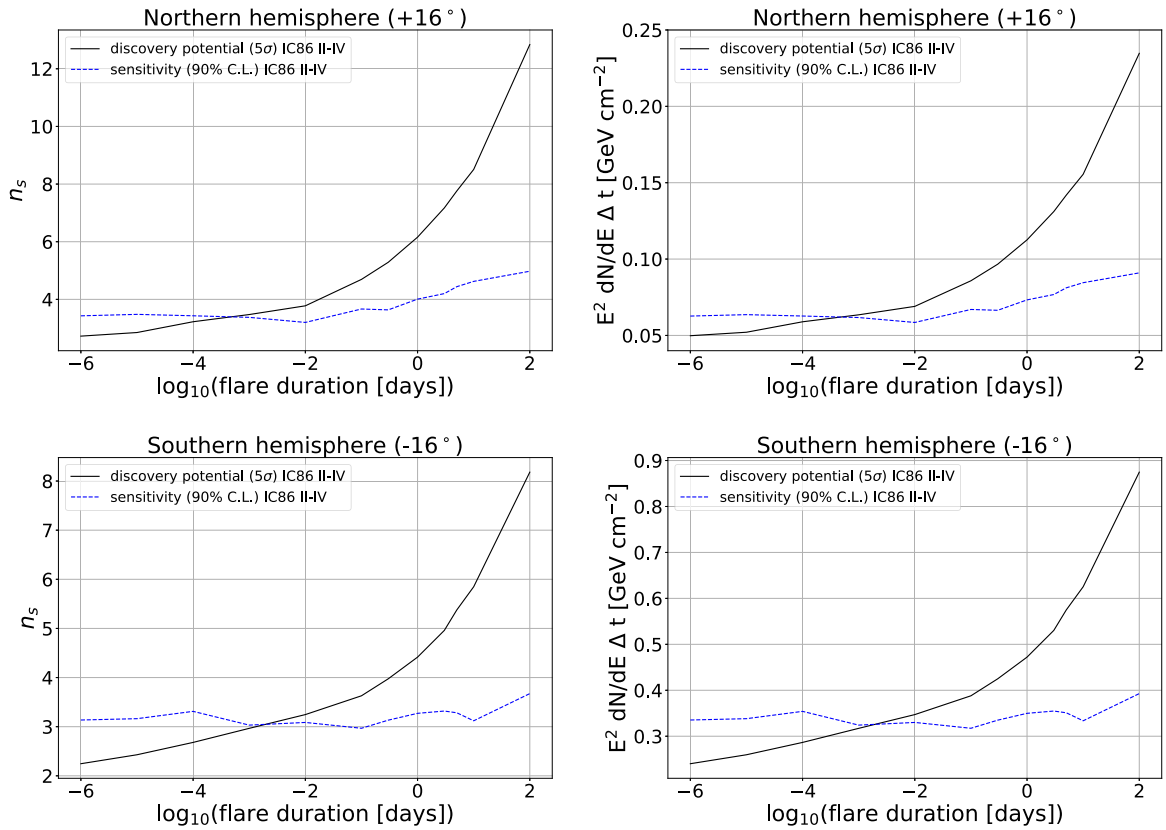

Figure 3. The 5σ discovery potential (solid black line) and the sensitivity (dashed blue line) for IC86 II-IV, shown in terms of the mean number of signal events (n_s) (left) and in terms of the time-integrated flux (right) for a fixed source in the Northern Hemisphere at $+16°$ in decl. (top) and in the Southern Hemisphere at $-16°$ (bottom), with an E^{-2} spectrum.

If we assume that the gamma-rays recorded in the light curve are produced via hadronic interactions of cosmic rays, a higher astrophysical neutrino flux is expected where a higher gamma-ray flux is detected. However, the neutrino background should stay constant. This provides an opportunity to restrict the search for astrophysical neutrinos to the periods of enhanced gamma-ray activity, thus maximizing the signal while reducing the background. The neutrino signal enhancement might be even larger during flares, since in many models of neutrino emission, the neutrino-production efficiency is actually doubly enhanced during flares, due to the fact that both the proton injection and the target photon field are expected to be enhanced at the same time (Oikonomou et al. 2019).

The flux level at which we consider the object to be in a flaring state is not well-defined. The threshold, which is a parameter of the fit, determines where the source is considered to be in a flaring state, since it results from the likelihood method optimization of the signal over background. The construction of the signal time PDF from the variation of the threshold is illustrated by Figure 6. Below the threshold, the time PDF is defined as zero. Above the threshold, the time PDF is defined by the area of the light curve normalized to one, as shown in Figure 6(b). The value of the threshold is varied during the likelihood maximization.

The test statistic is defined as

$$TS = -2\log\left[\frac{\mathcal{L}(n_s = 0)}{\mathcal{L}(\hat{n}_s, \hat{\gamma}_s, \hat{D}_t, \hat{f}_{th})}\right], \tag{7}$$

with $\hat{n}_s$, $\hat{\gamma}_s$, $\hat{D}_t$, and $\hat{f}_{th}$ being the best-fit values for the number of signal events, the spectral index, the time lag, and the threshold of the time PDF, respectively. Notice that, in the fit, the parameter γ_s is allowed to vary between 1 and 4.

The 5σ discovery potential and the sensitivity of this analysis, shown in Figure 7, are functions of the value of the threshold, f_{th}, given in terms of flux. The discovery potential and the sensitivity are largely insensitive to the threshold, even though there is a small tendency for them to improve with larger threshold. The reason for this is that, the higher the threshold is, the more the time PDF is restricted to a short period and the less background is included in the fit. Logically, fewer events are needed in order to make a discovery in such case. An average of three events are required for a discovery, while about two events are needed to reach the 90% sensitivity level.

4. Results

4.1. Time-dependent All-sky Scans

4.1.1. IC86 II-VI Analysis

The all-sky scan is realized by running the fit, resulting in a *TS* (Equation (6)), at each point of a $0\overset{\circ}{.}1 \times 0\overset{\circ}{.}1$ grid over the sky (except the poles). Each *TS* is converted into a *p*-value, assuming that the *TS* distribution follows a χ^2 distribution of three degrees of freedom, even though four parameters are fitted in the analysis. Indeed, due to correlations between parameters and some having limited ranges, a χ^2 distribution of three degrees of freedom was found to be the one best

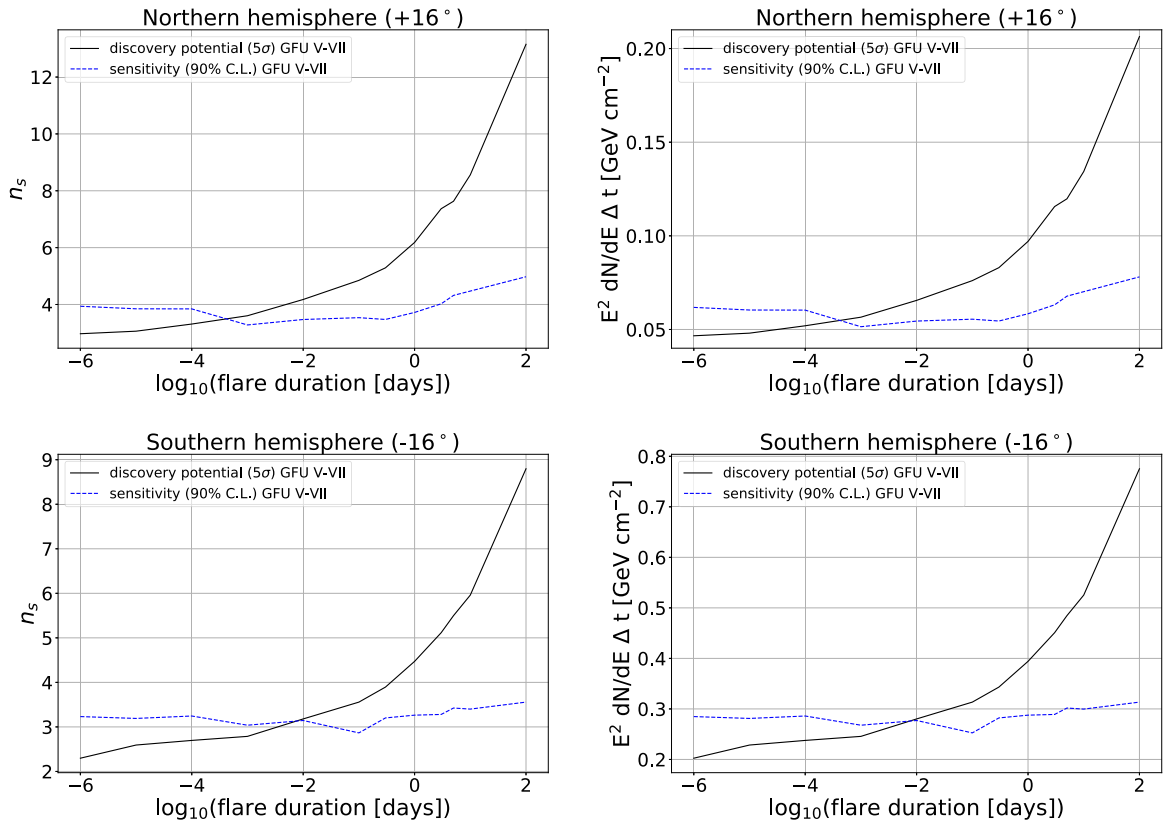

Figure 4. The 5σ discovery potential (solid black line) and the sensitivity (dashed blue line) for IC86 V-VII, shown in terms of the mean number of signal events (n_s) (left) and in terms of the time-integrated flux (right) for a fixed source in the Northern Hemisphere at $+16°$ in decl. (top) and in the Southern Hemisphere at $-16°$ (bottom), with an E^{-2} spectrum.

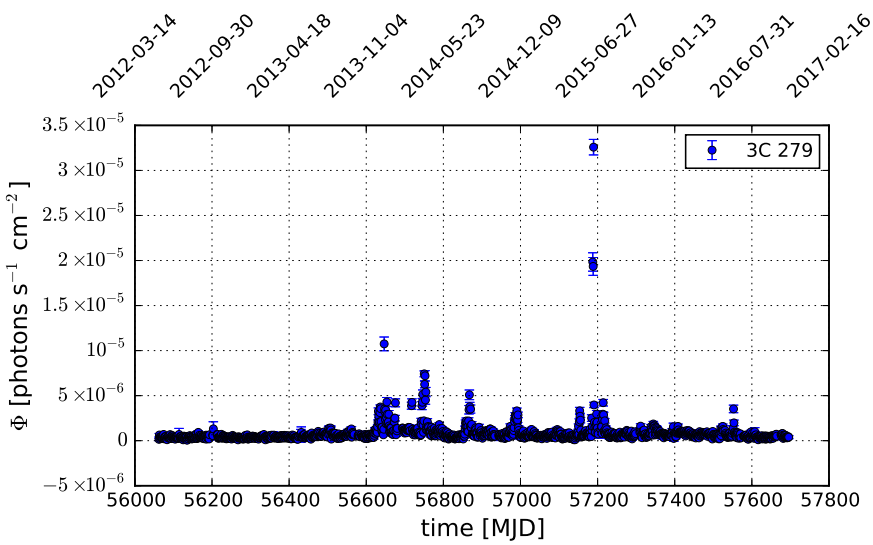

Figure 5. Integral photon flux above 100 MeV of the 3C 279 blazar with one-day binning, produced using aperture photometry. Data come from Fermi-LAT.

representing the *TS* distribution. Figure 8 shows a sky map of the entire sky in equatorial coordinates for the period from 2015 to 2017, and reports the *p*-value found at each point of the grid.

The *p*-values shown in the sky map are *pretrial* *p*-values. The most significant spot in each hemisphere is circled in black on the sky map in Figure 8. The hottest spot overall was found in the Northern Hemisphere at (R.A., decl.) = (170°.4, 28°.0).[65] The best-fit parameters of the Gaussian time PDF are $\hat{T}_0 = 56167.27$ MJD and $\hat{\sigma}_T = 40.01$ days. The fitted number of signal events is $\hat{n}_s = 11.79$, and the fitted spectral index is $\hat{\gamma} = 2.11$. The pretrial significance is 1.38×10^{-6}, which results in a posttrial *p*-value of 17.7%. The inferred posttrial *p*-value for the Southern Hemisphere is 24.2%. These values are compatible with a statistical fluctuation of the background. The observed *p*-values from the data, together with the distributions of *TS* from pseudo-experiments, are shown in the left panels of Figures 9 and 10.

[65] All equatorial coordinates are quoted for the J2000 epoch.

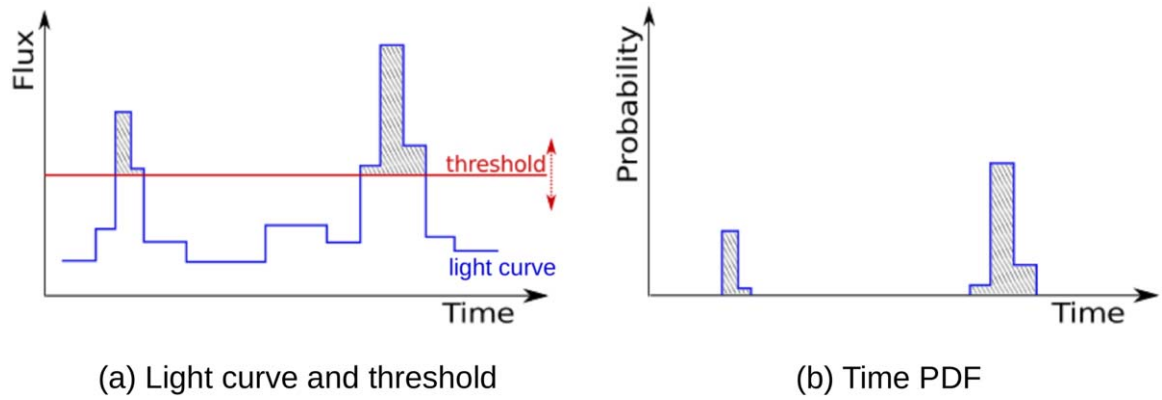

Figure 6. (a) The threshold (red) is varied within the flux range defined by the denoised gamma-ray light curve (blue). It defines a region where the source denoised gamma-ray light curve (blue) indicates a high-state. (b) The time PDF is constructed from the light curve and the value of the threshold.

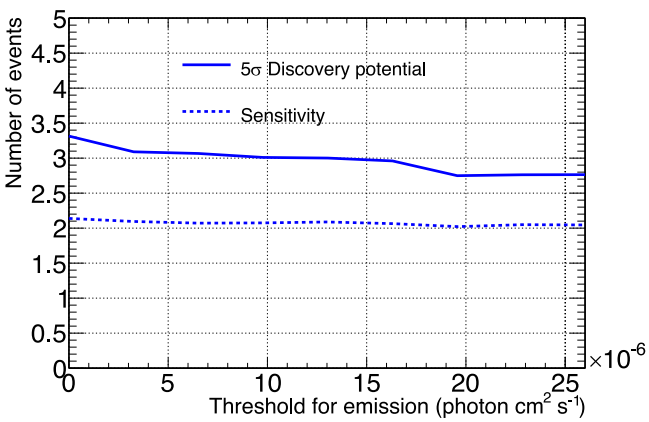

Figure 7. Sensitivity and 5σ discovery potential for the 11 day flare analysis in a number of neutrino signal events as a function of the gamma-ray threshold level in daily bins.

In order to help visualize how the different terms of the likelihood contribute to each event, a weight w_i is defined for each event as the ratio between the signal and background PDF of the event without the time term:

$$w_i = \frac{P_i^{\rm sig}(\sigma_i, \boldsymbol{x}_i|\boldsymbol{x}_s) \cdot \epsilon_i^{\rm sig}(E_i, \delta_i|\gamma)}{P_i^{bkg}(\phi_i, \theta_i) \cdot \epsilon_i^{bkg}(E_i, \delta_i)}. \quad (8)$$

When the weights are then plotted on the time axis, they immediately allow us to visualize which part of the likelihood (spatial/energy or time) dominates the significance. The right panels of Figures 9 and 10 show the time-independent weights (Equation (8)) at a source direction $\boldsymbol{x}_s$ defined by the hottest spots in the Northern and Southern Hemispheres, respectively. The best-fit Gaussian time structure with mean $\hat{T}_0$ and sigma $\hat{\sigma}_0$ is overlaid.

4.1.2. IC86 V-VII Analysis

The time period of 2015 to 2017 was treated separately from the previous time period because a different event selection was applied. Figure 11 shows the sky map for the period 2012 to 2015, displaying the pretrial p-values. The most significant value for each hemisphere is circled. The hottest region is found in the Northern Hemisphere, like in the previous analysis period, at coordinates (R.A., decl.) = (77°.7, 2°.6). The pretrial p-value is 1.3×10^{-6}, with the best-fit number of signal events being $\hat{n}_s = 25.27$ for a flux with spectral index $\hat{\gamma} = 2.55$, and the most significant time clustering centered at $\hat{T}_0 = 57573.85$ MJD, with a Gaussian width $\hat{\sigma}_0 = 189.6$ days. This results in a posttrial p-value of 18.8%.

The right panel of Figure 12 (13) shows the time-independent weights in blue, at a source direction $\boldsymbol{x}_s$ defined by the hottest spot in the Northern (Southern) Hemisphere and the associated best-fit Gaussian in black. The corresponding histograms of background trials and the observed p-value (vertical black dashed line) are displayed in Figure 12 (13) for the Northern (Southern) Hemisphere.

In Figure 12, we can see that the best-fit Gaussian encompasses almost the entire analysis period. Given that no finer structure is found, the fit tries to maximize the test statistics by including as much background as possible, hence the largest Gaussian width is preferred.

No significant excess is found in the Southern Hemisphere (Figure 13) with a post-trial p-value of more than 80%.

Table 2 summarizes the results for each data period and each hemisphere, listing the coordinates of the hottest spot, the best-fit parameters, and the pretrial and posttrial p-values. In both cases, the smallest p-values were observed in the Northern Hemisphere, where a longer duration flare with a harder emission spectrum was found. None of those results are significant.

4.1.3. Results of the Scans at the Location of TXS 0506+056

Aartsen et al. (2018b) performed a dedicated time-dependent analysis at the position of the blazar TXS 0506+056, (R.A., decl.,) = (77°.4, + 5°.7), motivated by the detection of IceCube-170922A, and found a 3.5σ excess (posttrial p-value = 3×10^{-5}), corresponding to 13 ± 5 signal events in the time period between 2012 and 2015. The excess does not appear significant in the present analysis, even though the data and the analysis method are the same. This is explained by the fact that this work scans the entire sky, while Aartsen et al. (2018b) solely inspected the TXS 0506+056 direction. Since a grid of $0°.1 \times 0°.1$ over the whole sky is analyzed, the final p-values are penalized by large trial factors, which reduce their significance. It is interesting to note that the second-most significant hot spot (pretrial p-value = 9.2×10^{-6}) of the 2012-2015 analysis is found at (R.A., decl.,) = (77°.55, + 5°.65), which is consistent with the location of TXS 0506+056. Moreover, applying the analysis at the exact TXS 0506+056 location as a further

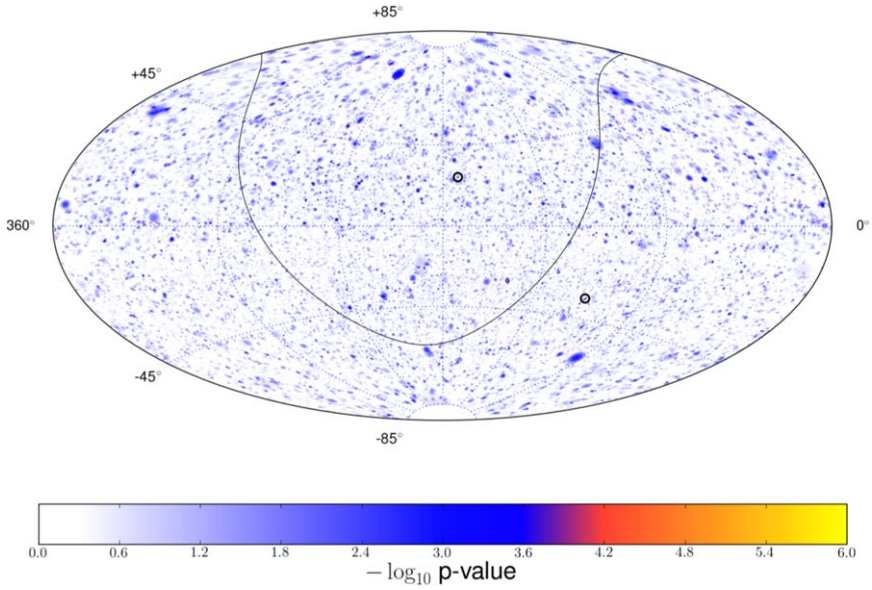

Figure 8. IC86 II-IV skymap in equatorial coordinates showing the pretrial p-values for the best-fit flare hypothesis tested in each direction of the sky. The strongest time-dependent Gaussian-like signal was found in the northern sky at (R.A., decl.) = (170.°4, 28.°0), with posttrial p-value of 17.7%. Solid black curve indicates the Galactic plane, and the hottest spot in each hemisphere is circled.

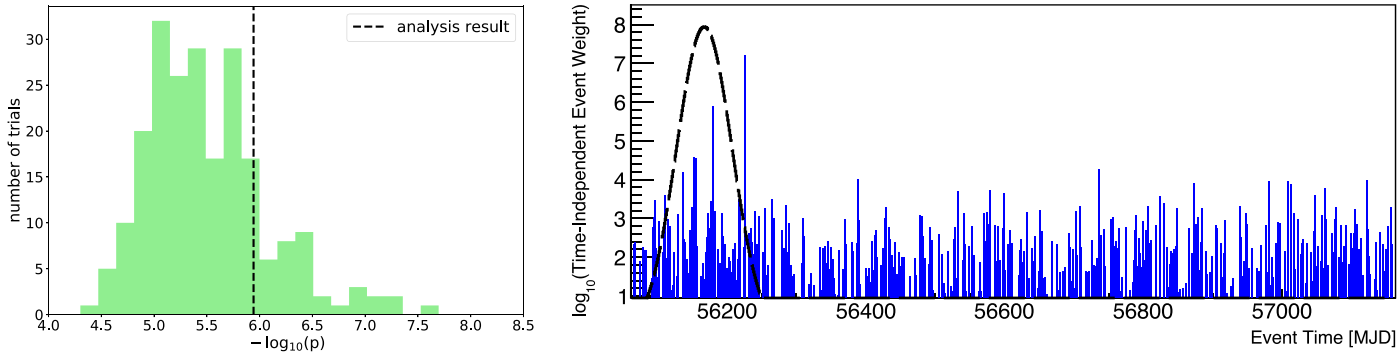

Figure 9. Northern Hemisphere. Left: Expected background p-value distribution obtained from scrambled data in green compared to the measured most significant pretrial p-value (shown as black vertical dashed line) in the northern sky. The inferred posttrial p-value is 17.7%. Right: Time-independent event weights, evaluated for the IC86 II-IV data in the Northern Hemisphere, at a source direction $\boldsymbol{x}_s$ defined by the hottest spot (R.A., decl.) = (170.°4, 28.°0). Best-fit Gaussian time PDF is shown in black (dashed), with mean $\hat{T}_0$ and sigma $\hat{\sigma}_0$.

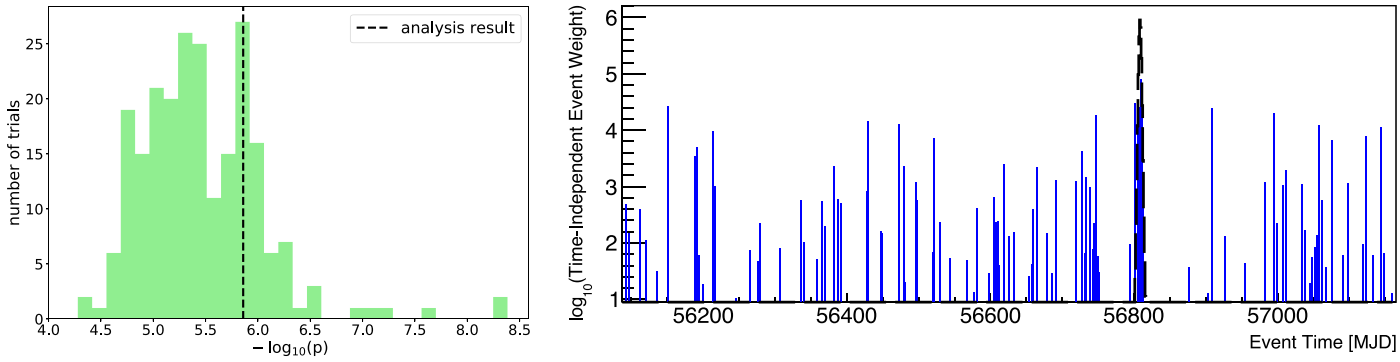

Figure 10. Southern Hemisphere. Left: Expected background p-value distribution obtained from scrambled data in green, compared to the measured most significant pretrial p-value (shown as the black vertical dashed line) in the southern sky. Inferred posttrial p-value is 24.2%. Right: Time-independent event weights, evaluated for the IC86 II-IV data in the Southern Hemisphere, at a source direction $\boldsymbol{x}_s$ defined by the hottest spot (R.A., decl.) = (89.°45, −35.°95). Best-fit Gaussian time PDF is shown in black (dashed), with mean $\hat{T}_0$ and sigma $\hat{\sigma}_0$.

check, this work finds an excess of events ($\hat{n}_s = 13.55$) similar to that reported by Aartsen et al. (2018b) in the time period of 2012 to 2015, with a pretrial p-value of 1.65×10^{-5} and a pretrial p-value of 3.2×10^{-2} in the time period of 2015 to 2017, consistent with the pretrial p-values found by Aartsen et al. (2018b).

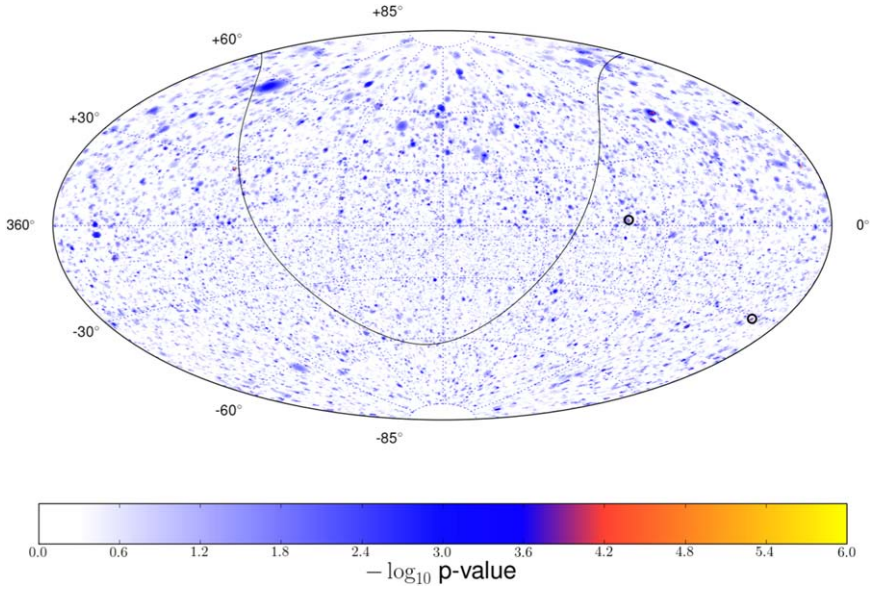

Figure 11. IC86 V-VII skymap in equatorial coordinates, showing the pretrial p-value for the best-fit flare hypothesis tested in each direction of the sky. The strongest time-dependent Gaussian-like signal was found in the northern sky at (R.A., decl.) = (77.°7 , 2.°6), with posttrial significance of 18.8%. Solid black curve indicates the Galactic plane, and the hottest spots are circled in each hemisphere.

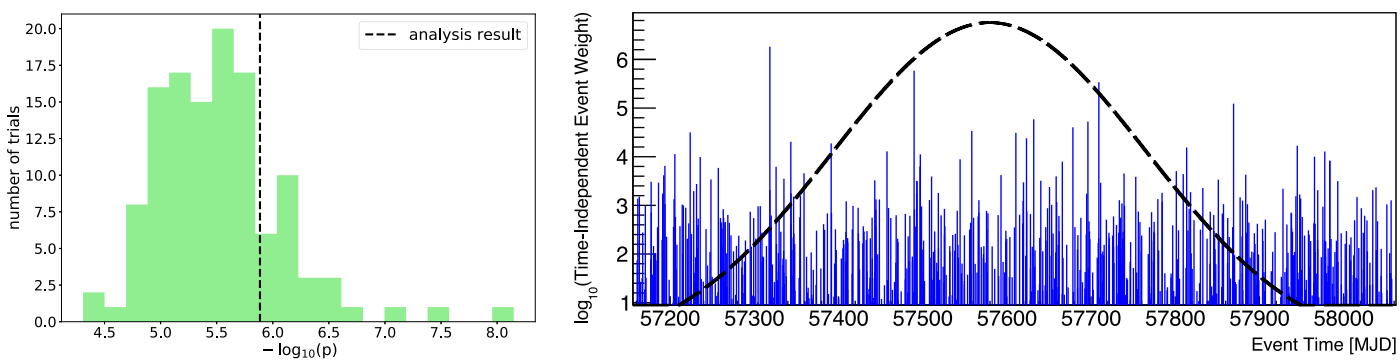

Figure 12. Northern Hemisphere. Left: Expected background p-value distribution obtained from scrambled data in green, compared to the measured most significant pretrial p-value (shown as the black vertical dashed line) in the northern sky. Inferred posttrial p-value is 18.8%. Right: Time-independent event weights, evaluated for the IC86 V-VII data in the Northern Hemisphere, at a source direction $\boldsymbol{x}_s$ defined by the hottest spot (R.A., decl.) = (77.°65, 2.°55). Best-fit Gaussian time PDF is shown in black (dashed), with mean $\hat{T}_0$ and sigma $\hat{\sigma}_0$.

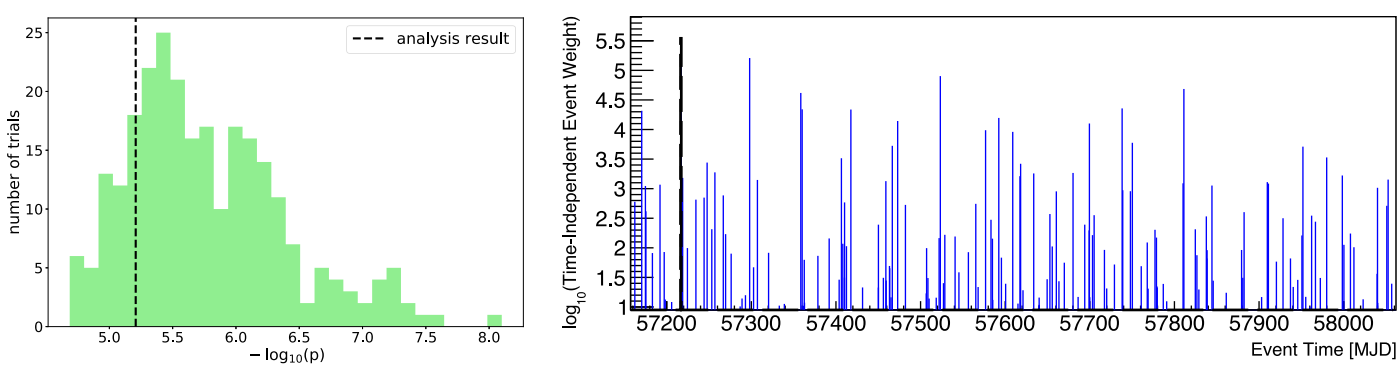

Figure 13. Southern Hemisphere. Left: Expected background p-value distribution obtained from scrambled data in green, compared to the measured most significant pretrial p-value (shown as the black vertical dashed line) in the southern sky. Inferred post-trial p-value is 81.5%. Right: Time-independent event weights, evaluated for the IC86 V-VII data in the Southern Hemisphere, at a source direction $\boldsymbol{x}_s$ defined by the hottest spot (R.A., decl.) = (9.°85, −31.°05). Best-fit Gaussian time PDF is shown in black (dashed), with mean $\hat{T}_0$ and sigma $\hat{\sigma}_0$.

4.2. 3C 279 Flare Analysis

This analysis looks for high-energy neutrino candidate events clustered in space around 3C 279, which is located in the southern sky at (R.A., decl.) = (194.°047, −5.°789), and in the time period defined by the blazar gamma-ray light curve. The result of the analysis is shown in Figure 14. The left panel displays the background TS values found by running the analysis on 10^6

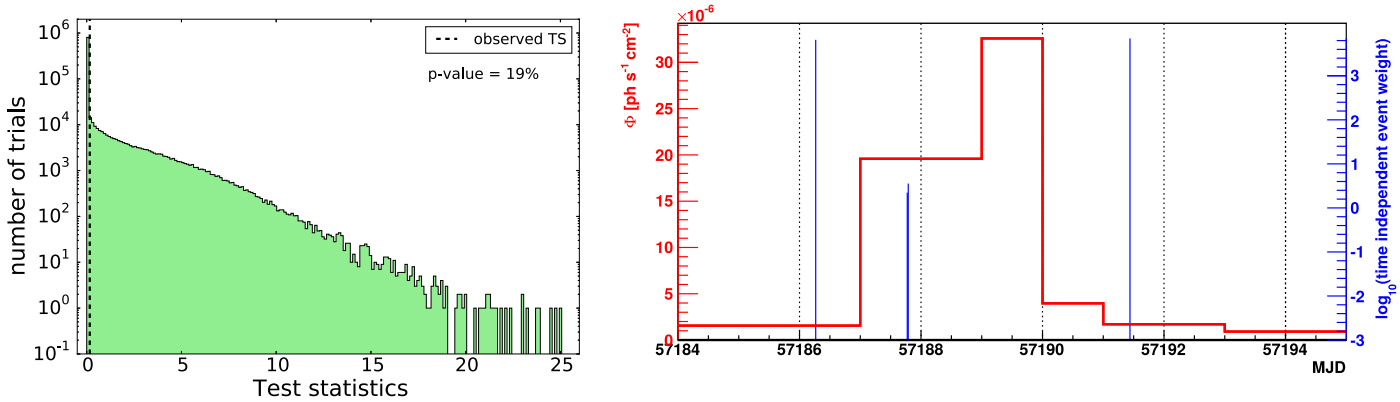

Figure 14. Result of the 11 day (MJD 57184-57195) analysis. Left: Test statistics for 10^6 background trial scrambled data in green. Black dashed line shows the *TS* value resulting from the analysis. Right: Red line is the denoised light curve of 3C 279. Blue vertical lines represent IceCube events selected by the analysis, and their size is given by the product of the signal over the background spatial and energy PDFs. The threshold is not represented, because it was fitted to zero. No correlation is found between the flare of 3C 279 and neutrinos detected by IceCube.

Table 2
Summary of All-sky Scan Results

Data set	R.A. (J2000) (°)	Decl. (J2000) (°)	Number of Signal Events $\hat{n}_s$	Spectral Index $\hat{\gamma}$	Gaussian Mean $\hat{T}_0$ (MJD)	Gaussian Width $\hat{\sigma}_T$ (days)	*p*-value Pretrial	*p*-value Posttrial
IC86 II-IV								
South	89.45	−35.95	7.48	2.85	56808.46	4.013	1.38×10^{-6}	24.2%
North	170.35	27.95	11.79	2.11	56167.27	40.01	1.14×10^{-6}	17.7%
IC86 V-VII								
South	9.85	−31.05	2.99	3.55	57216.78	0.021	6.19×10^{-6}	81.5%
North	77.65	2.55	25.27	2.25	57573.85	189.6	1.3×10^{-6}	18.8%

Table 3
Results of the 3C 279 Flare Analysis

Number of Signal Events $\hat{n}_s$	Spectral Index $\hat{\gamma}$	Threshold (photons cm^{-2} s^{-1})	Lag (days)	Test Statistic	*p*-value
0.48	2.45	0	0.5	0.16	19%

scrambled data sets. The result of the analysis performed on real data is marked with the black vertical dashed line. A final *p*-value of 19% is obtained, which is compatible with the background.

The right panel of Figure 14 shows the time-independent neutrino event weights as defined by Equation (8). The best-fit value of the threshold is 2.44×10^{-15} photons cm^{-2} s^{-1}, which is consistent with zero. This means that the time PDF is above this value and includes all 11 days. Table 3 summarizes the best-fit values of the parameters. The best-fit number of signal events is $\hat{n}_s = 0.48$, the spectral index $\hat{\gamma}$ is 2.45, and the lag was fit to its maximum value, i.e., 0.5 day.

Four events are visible in the right plot of Figure 14, but a total of nine contributed to the likelihood. However, their time-independent weight is so small that they are not represented in the plot. One may notice that two events around 57188 MJD are quite close in time. More details about these nine events can be found in Table 4, which shows the time, coordinates, weights, and visible reconstructed muon energy of each detected event in the 11 day analysis.

The spatial distribution of the events found in ±5° around 3C 279 is shown in Figure 15. The position of 3C 279 is marked with a red cross. The color scale represents the energy weight, while the circles show the angular error associated with each event. The four events that are the closest to the source have the highest energy and a fairly good angular precision, and these are the ones seen in Figure 14.

4.3. Upper Limit on a Hadronic Model

The number of neutrinos expected to be detected at IceCube in association with the huge flare of 3C 279 is estimated by Halzen & Kheirandish (2016), for a purely hadronic gamma-ray production mechanism. Considering the one day of highest emission of 3C 279 and taking into account IceCube's efficiency, the authors find that about four (two) events should be detected in time and space coinciding with the blazar flare for *pp* ($p\gamma$) interactions. Since this analysis did not find any excess of neutrinos following the gamma-ray time profile from the direction of the blazar, we can constrain the emission model of Halzen & Kheirandish (2016) by setting an upper limit on the number of neutrino events emitted by the source.

Halzen & Kheirandish (2016) assume that the observed gamma-rays in the MeV–TeV energy range are produced in a hadronic scenario, i.e., from protons colliding with radiation or

Table 4
IceCube Events Contributing to the Likelihood Fit, at the Position of 3C 279, in the Time Period MJD 57184–57195

Event time (MJD)	w_i ($\log_{10}$(spatialWeight · energyWeight))	R.A. (J2000) (°)	Decl. (J2000) (°)	Angular Error (1σ) (°)	$\log_{10}(E_\mu(\mathrm{GeV}))$
57185.41	−6.13	194.91	−3.35	0.37	2.81
57185.72	−2.98	190.00	1.56	1.59	2.75
57186.27	3.82	193.95	−4.99	0.46	3.26
57187.77	0.35	187.34	−4.69	1.91	3.07
57187.79	0.55	195.35	−3.89	0.57	3.10
57189.15	−3.30	187.78	12.07	3.73	2.87
57189.50	−3.50	197.67	−1.82	0.94	2.87
57191.44	3.85	194.95	−6.02	0.60	4.01
57194.61	−3.81	195.93	2.15	1.44	2.89

gas surrounding the blazar. In this mechanism, charged and neutral pions are created and decay in turn, producing neutrinos and high-energy gamma-rays. In order to derive the expected number of neutrinos that should be detected in IceCube, the neutrino flux must first be related to the observed gamma-ray flux. Following estimates (Halzen & Hooper 2005) and using energy conservation, one can write:

$$\int_{E_\gamma^{\min}}^{E_\gamma^{\max}} E_\gamma \frac{dN_\gamma}{dE_\gamma} dE_\gamma = K \int_{E_\gamma^{\min}}^{E_\gamma^{\max}} E_\nu \frac{dN_\nu}{dE_\nu} dE_\nu, \tag{9}$$

where the gamma-ray spectrum is defined as

$$\frac{dN_\gamma}{dE_\gamma} = A_\gamma E_\gamma^{-\alpha}, \tag{10}$$

where

$$A_\gamma = \frac{F_\gamma}{\int_{E_\gamma^{\min}}^{E_\gamma^{\max}} E_\gamma^{-\alpha} dE_\gamma}, \tag{11}$$

with $\alpha = 2.1$ being the measured spectral index, $F_\gamma = 24.3 \times 10^{-6}$ photons cm^{-2} s^{-1} the average daily flux during the one day of highest emission (Ackermann et al. 2016), $E_\gamma^{\min} = 0.1$ GeV, and $E_\gamma^{\max} = 300$ GeV. The factor K indicates the ratio between the number of gamma-rays and the number of neutrinos. For proton interactions with radiation, $K_{p\gamma} = \frac{\mathrm{BR}_\gamma}{\mathrm{BR}_\nu} = \frac{5/8}{3/8} = 1.7$, and for pp interactions, $K_{pp} = \frac{\mathrm{BR}_\gamma}{\mathrm{BR}_\nu} = \frac{1/2}{1/2} = 1$. BR_γ and BR_ν are the branching ratios of gamma-rays and neutrinos, respectively. They are calculated in the same way as in Halzen & Kheirandish (2016), the only difference being that we also consider synchrotron radiation or Compton scattering from the positrons produced by charged pions, which produces additional gamma-rays.

The neutrino spectrum is derived from Equation (9):

$$\frac{dN_\nu}{dE_\nu} \approx A_\nu E_\nu^{-2} \approx \frac{A_\gamma E_{\gamma,\min}^{-\alpha+2}}{(\alpha - 2) K \ln(E_{\nu,\max}/E_{\nu,\min})} E_\nu^{-2}. \tag{12}$$

Following the steps described in Halzen & Kheirandish (2016) and integrating Equation (12), the expected number of muon neutrinos in IceCube is

$$N_{\nu_\mu+\bar{\nu}_\mu} = t \int_{E_\nu^{\min}}^{E_\nu^{\max}} \frac{1}{3} \frac{dN_\nu}{dE_\nu} A_{\mathrm{eff}}(E_\nu, \delta) dE, \tag{13}$$

where we choose $t = 86{,}400$ s, 1 TeV $\leqslant E_\nu \leqslant$ 10 PeV, and the decl. band of 3C 279, $-6\overset{\circ}{.}289 \leqslant \delta \leqslant -5\overset{\circ}{.}289$. The factor $\frac{1}{3}$ accounts for neutrino oscillations. Here, $A_{\mathrm{eff}}(E_\nu, \delta)$ is IceCube's effective area at the decl. of 3C 279 and is shown by the dashed green line in Figure 2.

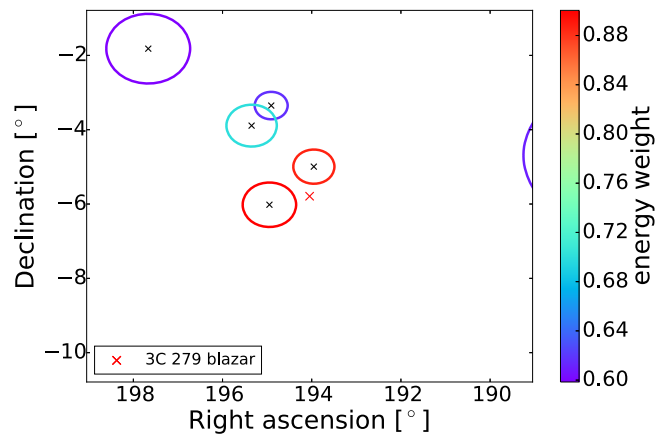

Figure 15. Location in decl. and R.A. of the IceCube events detected during the 11 days of the analysis. Here, 3C 279 is represented by the red cross. Color scale shows the energy weight. Circles show the angular uncertainty (i.e., paraboloid sigma; see Section 2). Nine events are detected in total, but five have a weight close to zero, which probably means background.

In order to compare against the model of Halzen & Kheirandish (2016), a 90% C.L. upper limit is calculated with the 3C 279 flare analysis. In this calculation, the injected signal is defined by a point source at the location of 3C 279 emitting a flux proportional to E^{-2}, having a fixed high threshold in order to effectively reduce the emission time to the same assumed in Halzen & Kheirandish (2016), corresponding to one day on 2015 June 16, when the highest emission was observed. The signal strength at which 90% of pseudo-experiments had a larger TS than the observed value corresponds to a mean of 2.18 signal events, which is slightly larger than the number of events needed to reach the sensitive region. This number of events translates to a time-integrated flux of $E^2 \frac{1}{A_{\mathrm{eff}}} \frac{dN}{dE} = 4.24 \cdot 10^{-2}$ GeV cm^{-2}.

The expected number of muon neutrino tracks in IceCube, $N_{\nu_\mu+\bar{\nu}_\mu}$, is calculated from Equation (13). Following the approach of Halzen & Kheirandish (2016), different neutrino energy ratios, $E_{\nu,\max}/E_{\nu,\min}$, which represent the energy interval over which proton interactions produce gamma-rays from pions, are tested and shown in Figures 16 and 17. The minimum neutrino energy, $E_{\nu,\min}$, is derived directly from the minimum energy of the protons, which depends on the value of the Lorentz factor of the jet of the blazar that is considered. The exact calculations are described by Equations (4) to (7) in Halzen & Kheirandish (2016). Once $E_{\nu,\min}$ is set, $E_{\nu,\max}$ is determined from the chosen neutrino energy ratio.

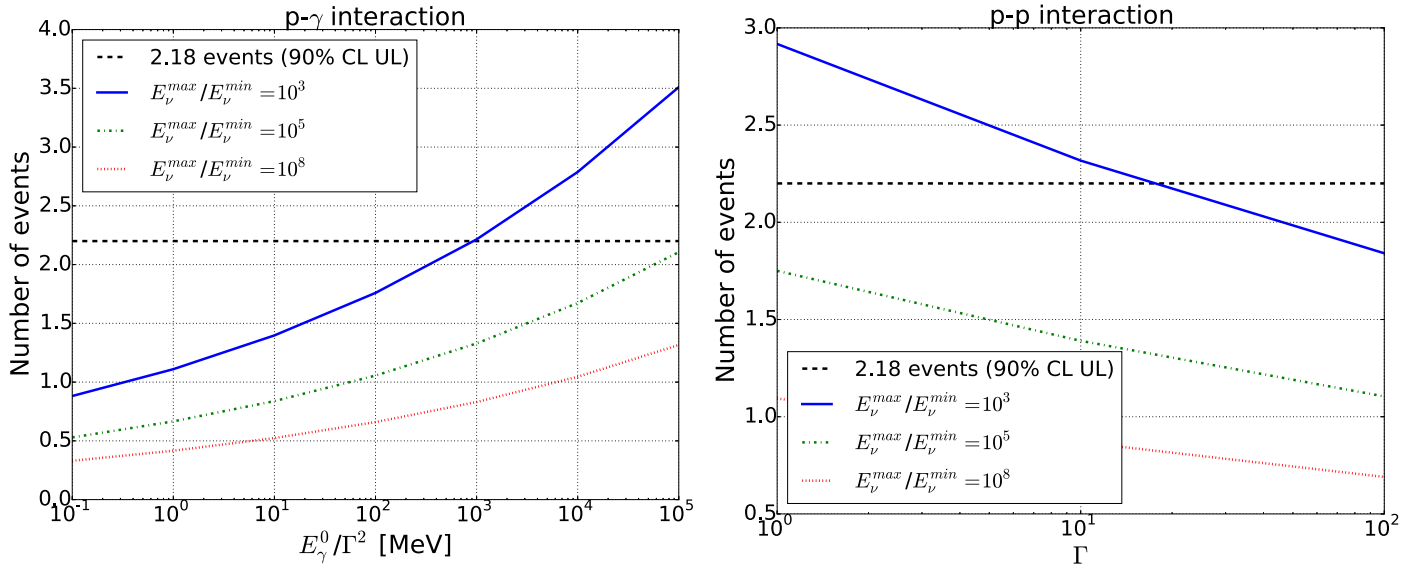

Figure 16. Left: Number of expected muon neutrino tracks in IceCube for $p\gamma$ interactions vs. E_γ^o/Γ^2, with E_γ^o being the energy of the target photons as derived from Halzen & Kheirandish (2016). Different colors represent different energy ranges where neutrinos are produced. Black dashed line represents the 90% CL upper limit corresponding to the one-day block on June 16 derived from the analysis. Parameter space above the dashed line is excluded. Right: Number of expected muon neutrino tracks in IceCube vs. jet Lorentz factor Γ in the case of *pp* interactions, as derived in Halzen & Kheirandish (2016). Different colors represent different neutrino production energy ranges. Black dashed line represents the 90% CL upper limit corresponding to the one-day block on June 16 derived from the analysis. The parameter space above the dashed line is excluded.

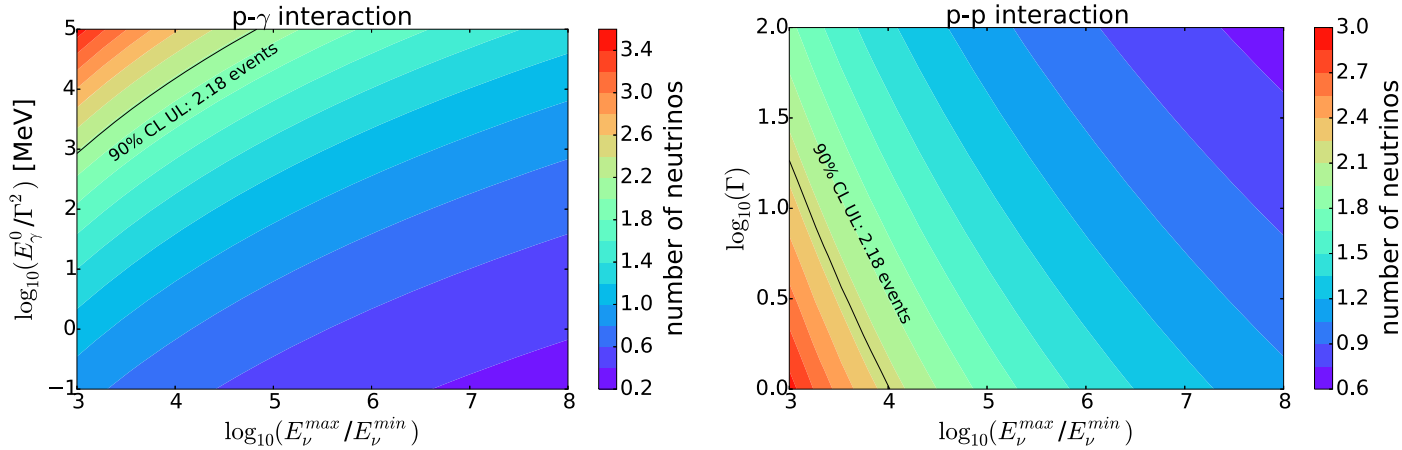

Figure 17. Contour plots showing the expected number of muon neutrino tracks in IceCube for $p\gamma$ (left) and for *pp* (right) interactions. Black line represents the 90% CL upper limit corresponding to the one-day block on June 16 derived from the analysis. The parameter space to the left of the black line is excluded.

Figure 16 shows the number of expected muon neutrino tracks in IceCube as a function of the Lorentz factor of the jet of the blazar Γ in the case of *pp* interactions (right) and as a function of E_γ^o/Γ^2, with E_γ^o being the energy of the target photons, in the case of $p\gamma$ interactions (left). The blue line corresponds to $E_{\nu,\max}/E_{\nu,\min} = 10^3$, the green line to $E_{\nu,\max}/E_{\nu,\min} = 10^5$, and the red line to $E_{\nu,\max}/E_{\nu,\min} = 10^8$. The black dashed line represents the 90% CL upper limit corresponding to the one-day block on June 16 derived from this analysis. Model parameters that lie above the dashed line are excluded.

Only a small fraction of the parameter space can be excluded by this analysis, assuming the smallest ratio, $E_{\nu,\max}/E_{\nu,\min}$, which represents the energy interval over which proton interactions produce gamma-rays from pions. In the case of $p\gamma$ interactions, large E_γ^o/Γ^2 ($>10^3$) can be excluded, while for the *pp* scenario, small Γ (<20) are disfavored.

Figure 17 gives the same information as Figure 16 in two dimensions. The colored regions correspond to the expected number of events. The parameter spaces to the left of the black lines are excluded.

5. Summary

In this paper, we reported a time-dependent all-sky scan on IceCube data from 2012 to 2017. The analysis searches each direction in the sky for an excess of neutrino events in space and time above the expected background. No assumptions are made regarding the potential sources of neutrinos. The most significant result in the period 2012–2015 corresponds to a *p*-value of 17.7%, which is compatible with background. It is obtained at the beginning of the analyzed period, the best-fit Gaussian time structure having its mean on 2012 August 28 and a width of 40 days, and it lies in the Northern Hemisphere at the position (R.A., decl.) = (170°.4, 28°.0), which is not close to any known

neutrino source. In the second analysis period, from 2015 to 2017, the most significant point is again located in the Northern Hemisphere, at coordinates (R.A., decl.) = (77°.7, 2°.6), with an associated p-value of 18.8%. While this location in the sky is only 3° away from TXS 0506+056, the largely insignificant result from the scan at the exact blazar position (see Section 4.1.3) suggests a mere background fluctuation at a location coincidentally close to the source.

Within the analyzed period, the blazar 3C 279, already well-known for its high variability, went through a brief but extremely intense gamma-ray flare that was recorded by the Fermi-LAT experiment. In order to analyze this interesting event, a dedicated time-dependent search was performed at the location of the blazar and during 11 days around the peak of the flare, which happened on 2015 June 16. Assuming that the neutrino emission would follow the intensity of the detected gamma-rays, we defined the signal time PDF directly from the gamma-ray light curve of 3C 279, obtained from Fermi-LAT. The analysis resulted in a p-value of 19%, which is compatible with background.

The 90% C.L. upper limit for the day of most intense gamma-ray activity of the blazar was calculated and used to constrain the neutrino emission model presented in Halzen & Kheirandish (2016). This model, which is purely hadronic, estimates the number of neutrinos that should be detected by IceCube as function of the Lorentz boost of the jet of the blazar Γ and of the energy of the target photons E_γ^o. Different neutrino energy intervals over which proton interactions would produce gamma-rays from pions were calculated, and the results were expressed as a function of the neutrino energy ratio, $E_{\nu,\max}/E_{\nu,\min}$. Assuming the smallest ratio of neutrino energies leads to the most stringent limits, where large E_γ^o/Γ^2 ($>10^5$) are excluded in case of pγ interactions, while small Γ (<20) are disfavored for the pp scenario.

The IceCube collaboration acknowledges the significant contributions to this manuscript from Stéphanie Bron and Teresa Montaruli. The authors gratefully acknowledge support from the following agencies and institutions, listed by country. From the United States of America: the U.S. National Science Foundation–Office of Polar Programs, U.S. National Science Foundation–Physics Division, Wisconsin Alumni Research Foundation, Center for High Throughput Computing (CHTC) at the University of Wisconsin–Madison, Open Science Grid (OSG), Extreme Science and Engineering Discovery Environment (XSEDE), the Frontera computing project at the Texas Advanced Computing Center, the U.S. Department of Energy–National Energy Research Scientific Computing Center, the Particle astrophysics research computing center at the University of Maryland, the Institute for Cyber-Enabled Research at Michigan State University, and the Astroparticle physics computational facility at Marquette University. From Belgium: the Funds for Scientific Research (FRS-FNRS and FWO), FWO Odysseus and Big Science programmes, and the Belgian Federal Science Policy Office (Belspo). From Germany: Bundesministerium für Bildung und Forschung (BMBF), Deutsche Forschungsgemeinschaft (DFG), the Helmholtz Alliance for Astroparticle Physics (HAP), Initiative and Networking Fund of the Helmholtz Association, Deutsches Elektronen Synchrotron (DESY), and the High Performance Computing cluster of the RWTH Aachen. From Sweden: the Swedish Research Council, Swedish Polar Research Secretariat, Swedish National Infrastructure for Computing (SNIC), and the Knut and Alice Wallenberg Foundation. From Australia: the Australian Research Council. From Canada: the Natural Sciences and Engineering Research Council of Canada, Calcul Québec, Compute Ontario, the Canada Foundation for Innovation, WestGrid, and Compute Canada. From Denmark: the Villum Fonden and Carlsberg Foundation. From New Zealand: the Marsden Fund. From Japan: the Japan Society for Promotion of Science (JSPS), and the Institute for Global Prominent Research (IGPR) of Chiba University. From Korea: the National Research Foundation of Korea (NRF). From Switzerland: the Swiss National Science Foundation (SNSF). From the United Kingdom: the Department of Physics of the University of Oxford.

ORCID iDs

J. A. Aguilar https://orcid.org/0000-0003-2252-9514
M. Ahlers https://orcid.org/0000-0003-0709-5631
A. Balagopal V. https://orcid.org/0000-0001-5367-8876
S. BenZvi https://orcid.org/0000-0001-5537-4710
E. Bernardini https://orcid.org/0000-0003-3108-1141
F. Bradascio https://orcid.org/0000-0002-7750-5256
S. Bron https://orcid.org/0000-0002-6305-3041
P. Coppin https://orcid.org/0000-0001-6869-1280
P. Correa https://orcid.org/0000-0002-1158-6735
P. Dave https://orcid.org/0000-0002-3879-5115
J. J. DeLaunay https://orcid.org/0000-0001-5229-1995
A. Desai https://orcid.org/0000-0001-7405-9994
P. Desiati https://orcid.org/0000-0001-9768-1858
G. de Wasseige https://orcid.org/0000-0002-1010-5100
T. DeYoung https://orcid.org/0000-0003-4873-3783
J. C. Díaz-Vélez https://orcid.org/0000-0002-0087-0693
M. A. DuVernois https://orcid.org/0000-0002-2987-9691
P. A. Evenson https://orcid.org/0000-0001-7929-810X
A. Franckowiak https://orcid.org/0000-0002-5605-2219
J. Gallagher https://orcid.org/0000-0001-8608-0408
S. Garrappa https://orcid.org/0000-0003-2403-4582
T. Grégoire https://orcid.org/0000-0001-8711-1456
S. Griswold https://orcid.org/0000-0002-7321-7513
F. Halzen https://orcid.org/0000-0001-6224-2417
F. Henningsen https://orcid.org/0000-0002-0680-6588
A. Kappes https://orcid.org/0000-0003-1315-3711
T. Karg https://orcid.org/0000-0003-3251-2126
U. Katz https://orcid.org/0000-0002-7063-4418
A. Kheirandish https://orcid.org/0000-0001-7074-0539
H. Kolanoski https://orcid.org/0000-0003-0435-2524
F. Lucarelli https://orcid.org/0000-0002-9558-8788
R. Maruyama https://orcid.org/0000-0003-2794-512X
F. McNally https://orcid.org/0000-0002-0785-2244
T. Montaruli https://orcid.org/0000-0001-5014-2152
R. W. Moore https://orcid.org/0000-0003-4160-4700
H. Niederhausen https://orcid.org/0000-0002-9566-4904
M. U. Nisa https://orcid.org/0000-0002-6859-3944
E. O'Sullivan https://orcid.org/0000-0003-1882-8802
N. Park https://orcid.org/0000-0002-4282-736X
A. Porcelli https://orcid.org/0000-0002-3220-6295
W. Rhode https://orcid.org/0000-0003-2636-5000
B. Riedel https://orcid.org/0000-0002-9524-8943
D. Ryckbosch https://orcid.org/0000-0002-8759-7553
I. Safa https://orcid.org/0000-0001-8737-6825
A. Sandrock https://orcid.org/0000-0002-5875-1670
M. Santander https://orcid.org/0000-0001-7297-8217

S. Sarkar https://orcid.org/0000-0002-3542-858X
S. Sarkar https://orcid.org/0000-0002-1206-4330
K. Satalecka https://orcid.org/0000-0002-7669-266X
A. Schneider https://orcid.org/0000-0002-0895-3477
L. Schumacher https://orcid.org/0000-0001-8945-6722
J. Soedingrekso https://orcid.org/0000-0003-1011-2797
T. Stuttard https://orcid.org/0000-0001-7944-279X
I. Taboada https://orcid.org/0000-0003-3509-3457
F. Tenholt https://orcid.org/0000-0002-7156-7392
A. Turcati https://orcid.org/0000-0002-8050-7869
C. F. Turley https://orcid.org/0000-0002-9689-8075
J. Vandenbroucke https://orcid.org/0000-0002-9867-6548
N. van Eijndhoven https://orcid.org/0000-0001-5558-3328
J. Weldert https://orcid.org/0000-0002-3709-2354
N. Whitehorn https://orcid.org/0000-0002-3157-0407
T. Yuan https://orcid.org/0000-0002-7041-5872

References

Aab, A., Abreu, P., Aglietta, M., et al. 2017, Sci, 357, 1266
Aab, A., Abreu, P., Agliette, M., et al. 2018, ApJL, 853, L29
Aartsen, M., Ackermann, M., Adams, J., et al. 2014a, JInst, 9, P03009
Aartsen, M. G., Abbasi, R., Abdou, Y., et al. 2013a, Sci, 342, 1242856
Aartsen, M. G., Abbasi, R., Abdou, Y., et al. 2013b, ApJ, 779, 132
Aartsen, M. G., Abbasi, R., Ackermann, M., et al. 2014b, PhRvD, 89, 062007
Aartsen, M. G., Abraham, K., Ackermann, M., et al. 2016, ApJL, 824, L28
Aartsen, M. G., Abraham, K., Ackermann, M., et al. 2017a, ApJ, 835, 151
Aartsen, M. G., Ackermann, M., Adams, J., et al. 2014c, ApJ, 796, 109
Aartsen, M. G., Ackermann, M., Adams, J., et al. 2015a, PhRvD, 91, 022001
Aartsen, M. G., Ackermann, M., Adams, J., et al. 2015b, ApJ, 807, 46
Aartsen, M. G., Ackermann, M., Adams, J., et al. 2018a, Sci, 361, eaat1378
Aartsen, M. G., Ackermann, M., Adams, J., et al. 2018b, Sci, 361, 147
Aartsen, M. G., Ackermann, M., Adams, J., et al. 2019, EPJC, 79, 234
Aartsen, M. G., Ackermann, M., Aguilar, J. A., et al. 2017b, APh, 92, 30
Aartsen, M. G., Ackermann, M., Aguilar, J. A., et al. 2020, PhRvL, 124, 051103
Abbasi, R., Abdou, Y., Abu-Zayyad, T., et al. 2010, NIMPA, 618, 139
Abbasi, R., Abdou, Y., Abu-Zayyad, T., et al. 2011a, ApJ, 744, 1
Abbasi, R., Abdou, Y., Abu-Zayyad, T., et al. 2011b, ApJ, 732, 18
Abbasi, R., Ackermann, M., Adams, J., et al. 2009, NIMPA, 601, 294
Abeysekara, A. U., Archer, A., Benbow, W., et al. 2018, ApJL, 861, L20
Ackermann, M., et al. 2016, ApJL, 824, L20
Aller, H. D., Hughes, P. A., & Aller, M. F. 1987, in Superluminal Radio Sources, ed. J. A. Zensus & T. J. Pearson (Cambridge: Cambridge Univ. Press), 273
Atwood, W., Albert, A., Baldini, L., et al. 2013, arXiv:1303.3514
Baade, W., & Zwicky, F. 1934, PhRv, 46, 76
Braun, J., Baker, M., Dumm, J., et al. 2010, APh, 33, 175
Braun, J., Dumm, J., De Palma, F., et al. 2008, APh, 29, 299
Christov, A. 2016, PhD thesis, Geneva Univ., doi:10.13097/archive-ouverte/unige:91766
Cutini, S. 2015, ATel No. 7633
Halzen, F., & Hooper, D. 2005, APh, 23, 537
Halzen, F., & Kheirandish, A. 2016, ApJ, 831, 12
Hartman, R., Bertsch, D., Fichtel, C., et al. 1992, ApJL, 385, L1
Hayashida, M., Nalewajko, K., Madejski, G. M., et al. 2015, ApJ, 807, 79
Kidger, M. R., Garcia Lario, P., & de Diego, J. A. 1990, A&SS, 171, 13
Makino, F., Kii, T., Hayashida, K., et al. 1989, ApJL, 347, L9
Mannheim, K., Protheroe, R. J., Rachen, J. P., et al. 2001, PhRvD, 63, 023003
Maraschi, L., Ghisellini, G., & Celotti, A. 1992, ApJL, 397, L5
Neunhoffer, T. 2006, APh, 25, 220
Oikonomou, F., Murase, K., Padovani, P., Resconi, E., & Meszaros, P. 2019, MNRAS, 489, 4347
Resconi, E., Franco, D., Gross, A., Costamante, L., & Flaccomio, E. 2009, A&A, 502, 499
Scargle, J. D., Norris, J. P., Jackson, B., & Chiang, J. 2013, ApJ, 764, 167
Sikora, M., Stawarz, Ł., Moderski, R., Nalewajko, K., & Madejski, G. M. 2009, ApJ, 704, 38
Waxman, E., & Bahcall, J. N. 1999, PhRvD, 59, 023002